Tissue remodeling articulates the dynamics of mesodermal fate allocation during body axis morphogenesis

Charlene Guillot[1], Yannis Djeffal[2], Mattia Serra[3], Olivier Pourquie[2]
[1] Biology, iGReD, Clermont-Ferrand, France
[2] Genetics, Harvard Medical School, Boston, USA
[3] Physics, UC San Diego, La Jolla, USA

Introduction

In amniotes such as chicken or mouse, most embryonic tissues derive from a superficial epithelial layer of pluripotent cells called epiblast [1,2]. Cells from this tissue either become internalized in the primitive streak (PS) during gastrulation to form the endoderm and mesoderm or they remain superficial and give rise to ectoderm. Epiblast ingression starts in the PS which forms in the posterior region of the embryo and progressively extends anteriorly as gastrulation progresses. Gastrulation is often considered to last until full PS extension, when endodermal as well as heart, head mesoderm and notochord territories of the epiblast have ingressed. After it reached its maximal size, the PS begins to regress, laying in its wake the mesodermal territories of the trunk of the embryo which continue to ingress from the epiblast. This later phase of building the posterior part of the body has also been considered to represent the continuation of gastrulation [3-5].

The fate of epiblast cells has been identified with fate mapping experiments where cells were marked to track their descendants. This identified the contribution of epiblast regions to specific embryonic territories and the final fates of cells of these territories [6-21]. Fate mapping the epiblast adjacent to the regressing PS in chicken and mouse embryos established that the domain anterior to the PS gives rise to neural plate. The node, which marks the anterior tip of the PS, yields the prechordal plate and notochord. The anterior epiblast adjacent to the node and the anterior PS contains the neuro-mesodermal precursors (NMPs) which contribute both to paraxial mesoderm and spinal cord [15,22,23]. More posteriorly along the PS lie the trunk mesoderm presumptive territories. These are organized along the AP axis of the epiblast flanking the PS according to their future medio-lateral location in the embryo (Supplementary Figure 1) [7,8,14,18,24]. Thus, the territories of paraxial, intermediate, lateral plate and extraembryonic mesoderm are progressively found more posteriorly. Except for NMPs, most of these territories appear to be specified to fates restricted to one single germ layer [22,23]. During PS regression, these epiblast territories become progressively exhausted in a posterior to anterior direction until only the most anterior territory containing the NMPs and the node descendants, ie notochord precursors remains, contributing most of the tail bud progenitors Supplementary Figure 1) [22,25].

Epiblast fate maps identified regions of overlap between the different mesodermal fates [7]. Moreover, heterotopic grafting experiments as well as manipulating cell signaling demonstrated some level of plasticity of the epiblast [15,26-29]. Whereas fate maps usually characterize the fate of cell populations they provide limited information on the lineage of individual cells. Thus, whether these overlapping regions arise from a mixed population of fated progenitors or from cells with

broader developmental potential that can give rise to multiple mesodermal lineages remains undefined.

Here, combining grafting experiments with single-cell lineage analysis and tissue perturbations, we demonstrate that epiblast progenitors exhibit a broader developmental potential than suggested by fate maps. We show that cells normally fated to give rise to the lateral plate territory can also give rise to both neural and paraxial mesoderm lineages during primitive streak regression. This plasticity of epiblast cells is further supported by our scRNAseq data which demonstrates that except for NMPs, mesodermal progenitors of the different presumptive territories of the epiblast do not exhibit significant transcriptome differences and thus constitute a remarkably homogeneous population. Our data suggest that a distinct transcriptomic identity of the different mesodermal territories is only detected after their ingression in the PSM. Our experiments further suggest that these different identities are acquired in response to local cues which include mechanical signals.

Results:

Developmental plasticity of epiblast mesodermal precursors of the chicken embryo

We performed heterotopic and heterochronic transplantations of small regions of the epiblast of 1 to 3-somite chicken embryos to evaluate their developmental plasticity (Figure 1; Supplementary Figure 2). We transplanted a small domain from the anterior epiblast of the PS (NMP region) from Hamburger&Hamilton (HH) [30] stage 7-8 donors expressing GFP ubiquitously, into the prospective LP territory, at the mid-streak level of stage 5-6 HH unlabeled hosts (Graft1: G1) (Figure 1A-D). 20 hours after the graft, in 10 out of 10 embryos, the GFP-positive cells localized in the LP tissue indicating that grafted cells differentiated according to their novel environment (Supplementary Figure 2C). In 6 out of 10 embryos, no GFP cells remained in the tail bud progenitor domain indicating that the grafted cells did not self-renew (Figure 1C-D, Supplementary Figure 2C). We next assessed the identity of the transplanted GFP cells by immunofluorescence using known markers of the NMPs ($SOX2^+/TBXT^+$) [31], paraxial mesoderm ($MSGN1^+$) [22] and LP ($pSMAD1/5/9^+$) [32] fates (Figure 1I-Q). Cells of the NMP territory grafted in the LP domain produce LP-like descendants that are pSMAD1/5/9 positive (Figure 1I-M) but MSGN1 negative (Figure 1N-R). Thus, epiblast cells of the NMP domain can change fate and give rise to LP cells when grafted into the LP progenitor region of the PS.

We also performed the reverse type of grafts (Graft 2: G2) by transplanting a small fragment of the epiblast from the mid-streak level (corresponding to the LP progenitor domain) from a stage 7-8 HH GFP-expressing embryo to the anterior-most region of the PS (NMP domain) of a stage 5-6 HH host (Figure 1E, H). Following a 20-hour reincubation period, GFP-positive cells integrated the paraxial mesoderm in 12 out of 12 grafted embryos (Supplementary Figure 2D). In 10 out of 12 embryos, GFP cells were retained in the NMP domain of the tail bud (Figure 1G-H, Supplementary Figure 2D), suggesting that they can self-renew. The transplanted LP progenitors express NMP markers ($SOX2^+/TBXT^+$) and produce MSGN1-positive descendants when grafted into the NMP domain (Figure 1S-U). Few GFP cells were found in the neural tube in the G2 grafts. However, such was also the case in 5 out of 6 controls, where we performed homotopic and homochronic grafts of the same NMP territory from a stage 7-8 HH GFP donor into a stage-matched unlabeled host (Supplementary Figure 2B). This is most likely due to the short reincubation period using *ex ovo* culture as we previously showed that the bipotentiality of

NMPs is mostly expressed at later developmental stages (Figure 1A-H) [22]. Cells of the LP progenitor region appear therefore to switch to an NMP fate when grafted in the anterior epiblast. Together, these experiments show that cells from the NMP and LP domains of the PS epiblast are not committed to a specific cell fate at these stages. They respond to their novel environment by losing their original identity, acquiring markers appropriate to the fate of their novel location.

Limited heterogeneity of the transcriptome of epiblast cells

We next investigated the molecular basis of this developmental plasticity. To do so, we generated a single cell RNA sequencing (scRNAseq) dataset of the PS and adjacent epiblast region at stage 4HH, 5HH, 6 somites and 35 somites (Figure 2, Supplementary Figure 3-4). Using the inDrops pipeline [33], we generated single-cell transcriptomes of 11,812 cells from these 4 different embryonic stages. To identify cellular states, we developed a new unbiased clustering method based on differentially expressed genes, that can be used alongside known clustering methods such as Leiden or Louvain. This method, called Opticlust, considers the significance of the genetic profile of each identified cell population in our scRNAseq dataset (Figure 2A, left). Specifically, upon Leiden clustering, the resolution parameter is automatically determined such as all the clusters have a significant p-value for their first ranked differentially expressed genes.

We next used Opticlust to investigate the cellular composition of the epiblast and the mesoderm in our dataset. Up to the 6-somite stage, the epiblast forms the superficial epithelial layer adjacent to the PS, from which mesodermal derivatives will ingress. At stage 4HH, the only other epithelial layer of the embryo is the endoderm that lines its ventral part. At this stage, we identified one cluster enriched in genes such as *SOX17* indicating that it corresponds to endodermal cells (Figure 2B, Supplementary Figure 3A). Another epithelial cluster, characterized by expression of *EPCAM, CLDN1, PLPP1* most likely represents the superficial epiblast (Figure 2B supplementary Figure 3A). This cluster does not express the primitive streak marker *TBXT* but expresses *CDH1*, *POU5F3* (*OCT4*), [34] and *SFRP2* (Supplementary Figure 3B). This combination of genes characterizes the primed epiblast cell state *in vitro* and the epiblast cell state of the human Carnegie Stage 7 [35] which represents an approximately equivalent developmental stage to chicken stage 4HH. We thus named this cluster "epiblast". This epiblast cluster was still present at stage 5HH (Figure 2B, supplementary Figure 3C). At stage 5HH, we also detected another *CLDN1*-positive epithelial cluster which also expresses many genes enriched in NMPs (*TBXT, GJA1, DLL1, APCDD1, WLS, CDH2, ATP2B1, APLP2, WNT5A, WNT8A*) [22]. This cluster, which we called NMP, likely corresponds to the anterior-most epiblast adjacent to the Node and anterior PS. The NMPs are first detected in this territory at this stage. The third epithelial cluster detected at stage 5HH corresponds to the endoderm (*SOX17* and *GATA5*). We also identified a fourth epithelial cluster expressing genes associated with Neural Plate identity (*GBX2, HES5*) (Figure 2B, supplementary Figure 3C). At the 6-somite stage, the epiblast, NMP, and neural clusters were still present (Figure 2B Supplementary Figure 3D), but *POU5F3* (*OCT4*), and *SFRP2* were downregulated in the epiblast cluster (supplementary Figure 3B). In contrast, at the 35-somite stage, we could not detect any epiblast cluster except for an NMP cluster which we named NMP/TB since these cells localize in the tail bud at this stage (Fig2B, Supplementary Figure 3E). A neural (*CLDN1, GBX2, SFRP2*) cluster was also identified at the 6 and 35-somite stages while a surface ectoderm (*EPCAM, KRT7, KRT19*) cluster was found at the 35-somite stage.

We also identified clusters exhibiting identities of ingressed mesodermal cells. At stage 4HH, opticlust identified an extraembryonic mesoderm (*GATA5, KDR, SMAD6*) and a mixed mesoderm cluster expressing both paraxial identity markers, *GDF3*, *MSGN1, MEOX1* and lateral

plate mesoderm identity markers *(JAM3, MSX2* (Figure 2B, supplementary Figure 3) similar to the mixed mesodermal cluster identified in the mouse embryos at equivalent stages[36] (supplementary Figure 4B left). From stage 5HH on, opticlust identifies a Hensen's Node/notochord (*CHRD, NOTO)* cluster. At the 6-somite stage, the LP and PSM identities segregate into 2 clusters (Figure 2B; Table 1, Supplementary Figure 3D). Opticlust identifies a PSM cluster (*MSGN1, CHST15*) and an early LP cluster which expresses the epithelial marker *KRT18* (Table 1), and the LP markers (*MSX1/2, JAM3, BAMBI*) probably corresponding to newly formed LP which is epithelial at this stage. At the 35-somite stage, we identified mesodermal clusters including posterior PSM (*MSGN1*), anterior PSM/somite (*MEOX1, TCF15*), and LP (*MSX2, PRRX1, JAM3, ID2*). Intriguingly, no clear PS cluster was identified in our dataset, suggesting that PS and adjacent cells of the epiblast do not exhibit significant transcriptomic differences [37].

To confirm the consistency in annotations amongst individual datasets and compare their similarity across developmental time, we developed a pipeline called AIntegrate (Figure 2A). This tool utilizes a machine learning classifier to identify similarities between clusters at different timepoints and then displays a projection of the clusters at each timepoint on the merged UMAP containing all developmental times (Figure 2A, C, supplementary Figure 4B). The classifier analysis (supplementary Figure 4A, right) confirmed the similarity between clusters across different stages. It allowed us to confirm the identity of clusters found by opticlust in the merged dataset containing all stages (4HH, 5HH, 6 somites, and 35 somites) (Figure 2C).

Our results suggest that from the onset of PS regression at stage 4HH, the region of the epiblast fated to give rise to non-axial mesoderm contains only two cellular states including an NMP and a non-NMP state. The non-NMP epiblast is transient and disappears after the 6-somite stage. Using a classifier trained on a mouse embryo atlas, we found good agreement between our cellular states and those of the atlas (supplementary Figure 4A, left). Importantly, we find that the blue cluster (Figure 2C) matches the mouse mixed mesoderm identity (supplementary Figure 4A, white star) [38]. These results together with the projection of the mixed mesoderm clusters of stage 4 HH and 5 HH in the blue cluster UMAP region by the AI integrate algorithm (supplementary Figure 4A), suggest a mixed lateral/paraxial mesoderm identity of the first embryonic mesoderm cells produced after the beginning of PS regression. Thus, this clustering analysis indicates that the distinct mesodermal identities of epiblast territories are only acquired following ingression of multipotent precursors, probably in response to regional cues. Thus, the regionalized organization of the epiblast predicted from the fate maps (ie chordal, neuro-mesodermal, paraxial, intermediate, lateral, and extra-embryonic mesoderm) (supplementary Figure 1) is not reflected at the transcriptome level in our analysis.

Bioinformatics analysis reveals unexpected developmental trajectories of the epiblast/NMP cells

To understand how mesodermal cell fates diversify from the epiblast/NMP state, we developed a novel bioinformatics approach to study their developmental trajectories. We examined the relationship between cellular states identified in our scRNAseq dataset at all timepoints. To do so, we developed a program using the optimal transport model (Waddington-OT [39]) to predict cluster-to-cluster transitions. We call this trajectory hypothesis generator program CADOT (Cluster ADjusted Optimal Transport) (Figure 2A). Cells from all timepoints are distributed based on their transcriptional similarities in a 2D environment (ie UMAP), and all the calculated transitions between clusters are displayed on the graph using arrows that go from one cluster

(ancestor) to another (descendant). Additional information can be studied including the transition probability and the quantity of cells transported from one cluster to another. We chose stringent filter parameters such as unlikely transitions like anterior mesoderm/neural lineage transition are not represented. Visualization of the trajectories can be achieved using a Sankey diagram where the width represents the quantity of mass transported during a transition (Figure 2E) or directly in the UMAP (supplementary Figure 4C) with arrows indicating both mass transport (width of the arrow) and probability of the transition (color).

Using these filtering parameters, we first computed the hypothetic ancestors/descendants' relationships for epiblast cell states and their putative descendants by sub-clustering the ancestor cells: epiblast, NMP, and NMP/TB and descendant cells: neural, mixed mesoderm, LP, PSM Post, extraembryonic of stages 5HH, 6 somites, and 35 somites (Figure 2D, E and Supplementary Figure 4C). We analyzed lineage transitions from the epiblast to mesodermal clusters by computing transitions across two developmental windows from stage 5HH to 35 somites and from 6 somites to 35 somites to infer the immediate and long-term lineage trajectories of epiblast cells. This predicted well-known transitions identified in classical avian and mouse lineage studies. Interrogating CADOT to predict lineage trajectories from stage 5HH to 35 somites (Figure 2E, left) reveals that the epiblast cluster (grey) gives rise to PSM post (green), LP clusters (purple), NMP/TB and neural clusters. In addition, CADOT predicts a departing node from the NMP cluster to the NMP/TB cluster, which describes the maturation of NMP cells [22]. CADOT also identifies a transition from the NMP to the PSM fate recapitulating the short-term lineage fate mapping of this region in avian and mouse embryos [15,22]. From 6 somites to 35 somites (Figure 2E, right), CADOT also recapitulates known lineage transitions happening at these developmental times. From the NMP/TB node, which is the largest departing node, CADOT identifies transitions toward the PSM and neural clusters recapitulating the expected neuro-mesodermal bipotency of NMPs. Expected transition from epiblast to LP or the contribution of mixed mesoderm to PSM Post and LP are also identified. Altogether, this shows that CADOT accurately predicts expected developmental trajectories from the epiblast.

In parallel to these known transitions, CADOT also predicts previously undescribed trajectories departing from the NMP and the NMP/TB clusters with high probability. Specifically, we observe transitions from the NMP or NMP/TB to the LP fate (Figure 2E). This represents a truly novel differentiation trajectory for NMPs. Additionally, from stage 5HH to 35 somites (Figure 2E, left), lineage trajectories depart from the non NMP epiblast to neural and NMP/TB, suggesting that this epiblast can also give rise to these two lineages. These hypothetic trajectories again are consistent with the developmental potency of the epiblast observed in our grafts. Thus, our results hint at considerable plasticity of cells of the anterior and posterior epiblast domains.

Overall, our advanced trajectory pipeline combining Opticlust, AIntegrate, and CADOT, predicts known and novel ancestors/descendants' lineage trajectories. The most surprising results from CADOT predictions is the suggestion that both NMP and non-NMP epiblast cells can give rise to several cell fates beyond the neural and paraxial mesoderm lineages.

Single-cell lineage tracing identifies multipotent progenitors in the posterior epiblast domain.

Along its AP axis, the PS and its adjacent epiblast harbor specific domains fated to give rise to defined mesodermal populations (supplementary Fig1). These prospective mesodermal domains do not exhibit sharp boundaries and present a significant degree of overlap [7,14,26], raising the possibility of either the existence of mixtures of progenitors with distinct fates or of multipotent

progenitors at the boundary levels (Supplementary Figure 1B). To address this question, we investigated the lineage potency of single cells of the LP progenitor domain of the epiblast which lies at the mid-streak level between stages 4HH to 8HH. To track the fate of single cells of this region, we used a lineage tracing strategy based on the Brainbow-derived MAGIC markers [40]. We performed local co-electroporation of plasmids expressing a self-excising Cre recombinase and the Nucbow transgene together with the TolII transposase to drive transgene integration in epiblast cells. This strategy allows to permanently mark cell nuclei with a specific color code generated by the unique combination of different fluorescent proteins triggered by random recombination of the Nucbow cassette. This color code is then stably transmitted to each daughter cell and can be retrieved by confocal imaging and quantification of the color hues of cells in the electroporated embryos after a 48h reincubation period. Labeling cells at the mid-streak level at stage 5HH gave rise to descendant cells in the mesodermal (star), neural (square), and LP (circle) tissues (Figure 3A-F, supplementary Figure 5). Most of the cells were labeled in the region posterior to the forelimb at all anteroposterior (AP) levels (Figure 3B, C supplementary Figure 5) with many cells sharing the same color code in the paraxial mesoderm and LP (Figure 3D, E). Also, we found cells labelled in the neural tube (Figure 3F). Importantly, these cells present the same color codes distributed across several tissues such as neural tube and somite (Figure 3), or neural and lateral plate (Figure 3, Figure 3F, arrowheads). In 20 % of the 31 clones analyzed, we found cells with the same clonal identity in the neural tube, paraxial mesoderm and LP (Figure 3E-F, arrowheads). Thus, single cells of the 50% level of the PS at stage 5HH, which are classically considered fated to give rise to LP can give rise to descendants in multiple tissues of the posterior embryo including the neural tube (Figure 3F). In contrast, labeling the epiblast of the mid-streak level at stage 7-8 HH generated mostly LP cells (Figure 3G, H). Virtually no labeled cells were found in the neural tube or paraxial mesoderm when electroporation was performed at this stage. Thus, at stage 7-8 HH, cells of the mid-streak level are specified to the LP fate. These cells may however not be committed to this fate yet as they retain the potency to give rise to multiple germ layers as predicted by CADOT in the Sankey diagram (Figure 2E) and shown with the type 2 grafts (Figure 1E). Overall, our single-cell lineage tracing analysis indicates that at stage 5HH, epiblast cells of the mid-streak level are multipotent, generating neural, paraxial mesoderm, and LP lineages in the posterior embryo. In contrast, epiblast cells of the same PS level at stage 8HH mostly generate LP descendants.

Analysis of the tissue and cell dynamics identifies boundaries between territories of the epiblast

We next investigated collective cell movements and tissue remodeling in the epiblast, using the dynamic morphoskeleton analysis method [41]. This strategy allows to project onto the embryo the future dynamic behavior of cells. To perform this analysis, we first generated movies of the PS region of transgenic chicken embryos expressing GFP ubiquitously from stage 4^{+}HH to stage 8HH (Figure 4A supplementary Figure 6A-D). We then quantified tissue velocity fields using Particle Image Velocimetry analysis to identify regions where cells which are initially closely located diverge with time (repellers, Forward projection, FW) or where initially distant cells converge (attractors, Backward projection, BW) (Figure 4B-C). This analysis allows visualizing the future cell dynamics on the initial tissue configuration in the embryo (Figure 4D-E). We identified two significant repellers at stage 4^{+}HH: one which delimitates the mesodermal territory of the epiblast from the neural plate anteriorly (Figure 4D, F) and one that marks the boundary with the non-

neural ectoderm laterally (supplementary Figure 6B). We also identified one main attractor corresponding to the PS/ingressing zone towards which epiblastic cells converge (Figure 4C,E supplementary Figure 6C). Thus, our morphoskeleton analysis correctly delimitates the epiblastic territory of mesodermal precursors from future ectodermal domains (Figure 4F, supplementary Figure 6D). Remarkably, this analysis did not reveal any repellers separating the future mesoderm territories of the epiblast along the AP axis.

To increase the resolution of our analysis, we generated 10h movies of embryos labeled with the vital dye nuclear red (Figure 4G, H). This allows to sparsely label the nuclei of epiblast mesodermal progenitors to identify individual cell tracks (Figure 4H). Using these tracks with the morphoskeleton pipeline, we could identify 2 stable repellers forming orthogonally to the PS (Figure 4I-L). We named these repellers Boundary 1 and 2 (B1, B2) based on their timing of appearance during embryonic development (Figure 4L). B1 appeared at mid-streak level, 200 minutes after the beginning of PS regression (Figure 4M, N, U, V). The location and time (stage 6HH) at which this boundary forms maps to the level of the expected segregation of the embryonic and extraembryonic mesodermal domains of the epiblast (Figure 4N-O). Thus prior to B1 formation, epiblast cells at the mid-streak level can freely move in this region (Figure 4P). The presence of the B1 repeller, indicates that after stage 6HH, cells remain on each side of B1, becoming confined to the extraembryonic and embryonic (LP) mesoderm domains of the epiblast (Figure 4N, P).

B2 forms 301 minutes after the beginning of PS regression (stage 7-8 HH) at the 70% PS level (Figure 4Q, R, U, V). The location and time at which this boundary forms suggest that B2 separates LP from paraxial mesoderm progenitors in the epiblast (Figure 4 R-S). After B2 forms around stage 7-8 HH, cells remain confined on either side of the repeller (Figure 4 R, T) and will give rise either to LP or paraxial mesoderm descendants. Importantly, this dynamics of B2 formation parallels the fate restriction observed in our lineage tracing analysis of mid-streak progenitors. Cells electroporated before boundary formation (stage 5HH, Figure 3A) can give rise to different embryonic mesodermal fates. In contrast, the fate of cells electroporated after boundary formation at this level is restricted to the LP lineage (stage 7-8 HH, Figure 3G, H). Thus, while cells of the epiblast remain uncommitted as seen by our scRNAseq analysis and graft experiments, it is their physical confinement to a specific epiblast domain that eventually controls their specification to a specific lineage (Figure 4L). The morphoskeleton analysis also provides a dynamical view of the fate map formation in the epiblast complementing the static fate maps established by classical lineage tracing methods (Supplementary Fig1).

Displacement of epiblast progenitors depends on cell intercalation following cell division.

Our lineage tracing analysis indicates that mid-streak epiblast cells at stage 5HH can give rise to lineages normally derived from more anterior levels such as neural tube or paraxial mesoderm. One possible explanation for this surprising observation is that epiblast cells can move within the plane of the tissue to relocate more anteriorly during PS regression. Such free movement of cells is supported by our morphoskeleton analysis which did not identify repellers in the epiblast at this stage (Figure 4D). Since the epiblast is a pseudostratified epithelium, its cells are however expected to be constrained in their movements. One possibility is that cell division combined or followed by cell intercalation allows the displacement of daughter cells within the epiblast leading them to relocate and ingress in different domains and thus giving rise to different fates. To test this hypothesis, we performed live imaging of the epiblast of transgenic quail embryos expressing a

nuclear red (H2B-mCherry) [42] and green membrane fluorescent reporters (membrane-GFP) . We quantified the number of cell division events from 0 to 2 hours, 2 to 4 hours and 4 to 6 hours after the start of PS regression. We find around 126, 84, and 60 cell division events at these respective timepoints indicating more cell division events during the first hours of PS regression (Figure 5A). This is consistent with the results above finding higher tissue remodeling in the first hours of PS regression (Figure 4). Measuring the distance between sister cells at the end of cell division identified two distinct cell division patterns: non-intercalating sister cells (ie : 0 to 15um between daughter cells) and intercalating sister cells (more than 15um between daughter cells) (Figure 5B-D). Intercalation events upon cell division occurred mostly during the first 4 hours of PS regression (between stage 5 to 7-8 HH) in the first 700 microns of the anterior PS region (62 to 100% PS, Figure 5D, left). We observed limited number of intercalating daughter cells upon cell division in the more posterior region (750 to 1450 microns below the node) of the epiblast (20 to 58% PS, Figure 5D, right). These results support the existence of different cell division patterns in the epiblast during the early stages of PS regression. To test if the displacement of daughter cells within the epiblast supports their relocation and ingression in different domains to give rise to different fates, we tracked the position of sister cells originating from a mother cell anterior (grey dots) or posterior (black dots) to the mid streak B1 location (grey line) until their ingression during the mixing phase (0 to 240 min) (Figure 5 E,F). Cell tracks of sister cells emerging anterior to B1 ended up ingressing far away from each other while tracks from sister cells emerging posterior to the B1 location ingress closer to each other (Figure 5F). To further investigate the spatiotemporal ingression pattern of these epiblast sister cells we quantified the distance and time difference between the sister cells' ingression coordinates born anterior or posterior to B1 (Figure 5G). We find that cells born in the posterior streak region (posterior to B1), ingress on average 32um apart with a 19 min delay (Figure 5G). Thus, sister cells emerging from the predicted extraembryonic domain do not move very far apart meaning that they are likely to be exposed to similar environmental cues for cell fate decisions. Anterior to the B1 level (midstreak) we find a bimodal distribution of distance and time of ingression. Specifically, we observe that 30% of the sister cells ingress with a similar spatiotemporal dynamic as cells of the extraembryonic territory (16/52 cells ingress 50 um apart within the first 30 minutes after they were born) (Figure 5G, blue). In contrast, most sister cells born at the midstreak level ingress from 80 to 218 um apart with a delay between 50 to 135 min. Thus, the ingression dynamics of most sister cells born at or anterior to the midstreak level leads them to be exposed to distinct spatial and temporal cues that may explain the acquisition of different fates.

Thus, our results show that intercalation after cell division can affect the distribution of daughter cells within the epiblast during early stages of PS regression. Such displacements of progenitors in the epiblast may explain the cell pluripotency observed at mid-streak level in our cell lineage analysis.

Anterior and posterior epiblast cells are exposed to distinct mechanical constraints.

Our data indicate that despite being specified to the LP fate, cells of the mid-streak epiblast at stage 7-8 HH retain plasticity and can contribute to paraxial mesoderm when grafted at a more anterior level. This therefore suggests that external factors control the fate of these progenitors. One such set of factors which has been poorly investigated is the mechanical environment of the epiblast at these stages. To investigate the role of mechanical constraints in cell fate determination

in the epiblast, we first mapped tissue displacements and deformations using Particle Image Velocimetry analysis of the epiblast of stage 5HH to 9HH transgenic GFP embryos (supplementary Figure 6A, movie 1). To do so, we divided the tissue into a grid of 80um squares and followed their deformation over time. In the anterior PS domain, we observed a change in grid shape from a square to an enlarged and elongated diamond shape without loosing grid squares (white dots) (Figure 6A). This indicated important anisotropic deformations without tissue loss consistent with the cell intercalation observed. This also suggests the existence of pulling forces from neighboring tissues in both the anteroposterior and mediolateral directions (Figure 6A,B). The increased diagonal length of the diamond in this region of the grid indicates a greater deformation along the antero-posterior axis, marking the direction of anisotropy. Tissue loss seen by the disappearance of grid squares (pink dots) is visible anteriorly starting 4 hours (t=264 min) after the start of PS regression. Thus, we find massive anisotropic tissue rearrangement within the peri-node region and the anterior PS during the early stages of its regression (Figure 6A, B). In contrast, limited anisotropic deformations were observed in the more posterior PS region indicating that the epiblast undergoes deformation without shearing at this location. As expected from the known ingression flow of posterior epiblast, grid squares flanking the posterior part of the PS start disappearing from the beginning of PS regression indicating progressive tissue loss (pink dots). Hence, anterior and posterior PS domains are under different mechanical constraints with an expansion/remodeling zone in the anterior epiblast around the node and an ingression zone in the posterior epiblast (Figure 6A, B).

We next directly probed the forces within the anterior and posterior epiblast (Figure 6C) by monitoring the deformation of soft alginate gels inserted into these two epiblast regions *in ovo* (Figure 6C, supplementary figure 7A-C). We first performed a small ablation of a squared fragment of tissue (without removing the endodermal layer) at different AP positions along the PS in GFP transgenic embryos. We next implanted a small piece of alginate gel in the region of the ablation and measured the shape changes of the implant (Figure 6C-L, supplementary Figure 7A). In the anterior epiblast, we observed significant tissue relaxation in the mediolateral direction when cutting the tissue to place the gel implant indicating that this region is under high tension (Figure 6D, F, H, J). By quantifying the evolution of the gel implant shape over time we measured a 50% increase in the gel area 4 hours after placing the implant (Figure 6H, J). We observed an increase in length along the AP and ML axis with a bias toward a greater deformation along the AP axis (supplementary Figure 6B, C). These deformations are consistent with pulling forces from the neighboring tissues resulting in the anisotropic deformations described above (Figure 6A, B). 5 hours after placing the implant in the posterior epiblast domain, we observed a 50% decrease in the ML dimension indicating pushing forces from the mediolateral tissues (supplementary Figure 7C). In contrast, the gel AP length remained approximately constant (Figure 6E, G, I, J) (supplementary Fig7B). These results are consistent with the known convergence of the epiblast towards the PS leading to tissue ingression (Figure 4E, F). Thus, at the onset of PS regression, the anterior and posterior regions of the epiblast of the PS are exposed to different mechanical constraints. Pulling forces lead to epiblast remodeling anteriorly while ML compression associated with tissue ingression in the PS is observed posteriorly.

We next used aphidicolin to test the role of cell division on the dynamics of tissue remodeling, (Figure 6K, supplementary Fig7D-F). Using PIV analysis on treated embryos, we found that this treatment decreases the percentage of local anisotropic deformation within the epiblast particularly around the node region compared to WT (white dots, Figure 6K). Thus, hampering cell division specifically impairs tissue remodeling in the anterior domain (around the

node), but not posteriorly (white and pink dots). Importantly, morphoskeleton analysis on PIV measurement of aphidicolin-treated embryos identified a similar attractor region (supplementary Fig7D,E) indicating that cell division inhibition doesn't impact mesoderm ingression. However, unlike in WT embryos (right), repellers across the epiblast in a similar spatial and temporal location as B1 and B2 were visible in aphidicolin treated embryos using PIV analysis (arrows and dotted lines, supplementary Figure 7D, F) indicating that cell mixing impacts the formation of the boundary observed across the epiblast. Thus, our results show that cell division and tissue mechanics impact the position of the mesodermal progenitors within the epiblast, whether it also impacts their fate was studied next.

Interfering with epiblast mechanical properties affects mesoderm progenitors' fate

To directly test the impact of mechanical constraints in mesoderm progenitor fate decision *in ovo*, we placed a filter paper on top of the right epiblast parallel to the PS of embryos at stage 7-8 HH, and reincubated them for 5 to 12 h (Figure 7A,B,). We next tested how the filter affects tissue tension by cutting embryos along the PS in controls and in embryos with the filter (red stippled line). We tracked the dynamics of the cut opening using a kymograph visualization (black stippled line, Figure 7B, C). In controls, the cut opening increased, consistent with the existence of pulling forces from the neighboring tissues in the anterior epiblast (Figure 7C). On the contrary, in embryos with a filter, low relaxation is observed at the cut site (Figure 7C, right). Low relaxation is also observed in the AP direction in the filter and control conditions indicating limited significant changes in AP tension. Thus, placing the filter changes the mechanical properties of the epiblast, decreasing the ML pulling forces in the anterior region.

We next used this filter method without cutting the embryo followed by immunolabelling with TBXT and SOX2 antibodies to assess the identity of the descendants of the anterior epiblast cells exposed to this new mechanical environment. Placing the filter at stage 7-8 HH resulted in opened and buckled neural tube on the opposite side of the filter, indicating increased tension in the left side of the embryo (Figure 7D, E, supplementary Figure 8A-B). Surprisingly, we observed an increased number of NMP cells on the side lacking the filter (Figure 7D). Analyzing the intensity of TBXT/SOX2, in the NMP domain shows high SOX2 expression on the side lacking the filter and lower SOX2 on the filter side (Figure 7F) indicating that tissue tension impacts SOX2 expression in this progenitor domain. Moderate changes in TBXT expression were observed indicating that TBXT expression is less affected by tissue tension (Figure 7G). Thus, altering the mechanical properties of the epiblast can impact the number of SOX2/TBXT NMP cells changing the balance of progenitors forming the growing embryonic tissues.

We next tested how tissue tension affects the lineage of mesodermal progenitors of the epiblast. We electroporated a H2B::GFP transgene in both sides at the midstreak level of stage 7-8 HH embryo and placed the filter on the right side (Figure 7H, supplementary Figure 8C). Electroporated embryos were allowed to develop overnight. From our single-cell lineage tracing, we expect that electroporated cells ingress to give rise to LP cells in the mesoderm. Such is the case on the side lacking the filter where we observed GFP cells located in mesodermal tissues posteriorly (Figure 7 I, K, L) but no GFP cells in the NT anteriorly (Figure 7I-K). In contrast, we find that green electroporated cells on the filter side localize more anteriorly (Figure 7I, arrowhead) and integrate into the neural tube (Figure 7J, K, supplementary Figure 8D, E). Immunolabelling of these embryos shows that GFP-expressing cells can give rise to SOX2-positive cells in the neural tube on the filter side while no green cells are found at this AP location in the control side

(Figure 7J, arrowhead). This suggests that the electroporated cells are prevented from ingressing and remain in the epiblast eventually contributing to the neural tube. Hence changes in tissue tension affect the lineage of cells at mid-streak level so they now give rise to neural cells. Additionally, we find lower SOX2 expression on the filter side and disorganized tissue as seen by punctate and less defined cell contour of F-actin (Fig7 K, supplementary Figure 8D) compared to the contralateral side posterior to the neural tube, in the TBXT/SOX2 domain. Thus, our results demonstrate that changing the mechanical properties of the epiblast progenitors alters their fate and identity.

Discussion

Fate allocation is a central question of developmental biology. Historically, this has been investigated using coarse strategies involving the generation of fate maps tracking the position of precursors of the various territories of the adult body. These maps identified domains where cells are predicted to give rise to specific lineages. Strikingly, the boundaries of these territories are usually blurry during early stages of development. Thus, overlap between embryonic territories is usually the norm at least initially. Boundaries progressively sharpen as the embryo develops. Such is the case for the presumptive territories of the trunk mesoderm whose distribution along the AP axis of the epiblast lateral to the PS reflects their future fate along the medio-lateral axis (notochord, somites, lateral plate, blood/extraembryonic mesoderm) [7,14,24,26]. Initially, these domains significantly overlap at the level of their boundaries, raising the possibility of cell multipotentiality or of the existence of a mix of already committed progenitors in these regions.

Recent advancements in lineage tracing and single-cell transcriptome analysis now provide efficient tools to address this question at the single-cell level [39,43-45]. Such methodologies allowed to uncover the existence of bipotent NMPs in the perinodal region of the epiblast of amniotes [22,23]. Whether this multipotency extends beyond the NMP domain to other presumptive mesodermal domains of the epiblast remains an open question.

Understanding cell fate decisions requires to correctly identify cell types and their lineage relationships. While scRNAseq analysis can be used to infer developmental trajectories, which in many cases reflect the lineage history of cells, such is not always the case. These studies therefore need to be further validated by lineage tracing. The reconstruction of cell developmental history in silico using scRNAseq data first necessitates identification of cell identities which usually relies on clustering analysis. However, defining the clustering resolution is generally highly biased by preexisting knowledge of the development of these lineages. Here, we introduce a new suite of tools to analyze developmental trajectories. A first program called Opticlust uses the significance of differentially expressed genes to define clusters in a more unbiased fashion. We also developed another module called AIntegrates, which employs machine learning technologies to guide the annotation process. Finally, CADOT (Cluster ADjusted Optimal transport) can predict biologically relevant hypotheses regarding ancestor/descendant relationships. This new analysis pipeline aims to facilitate the prediction of cell fate transitions using single-cell RNA sequencing data.

Using this pipeline, we could predict ancestor/descendant hypotheses from the epiblast cell states, including both known and unknown transitions. Our analysis revealed that mesodermal progenitors within the epiblast become transcriptionally distinct over time while maintaining the

ability to give rise to multiple mesodermal cell types. We validated these trajectories through single-cell lineage tracing, demonstrating for the first time that cells from the midstreak level can give rise to neural, mesodermal, and lateral plate descendants. We also show that NMPs not only contribute to the paraxial lineage but can also give rise to LP. Our work provides evidence that mesodermal progenitors within the epiblast exhibit largely similar transcriptional profiles while maintaining pluripotent characteristics, rather than being a heterogeneous mixture of specified progenitors. Trajectory inferences in the mouse embryo identified several transcriptional trajectories giving rise to the somite lineage suggesting molecular flexibility during early cell type specification (GUIBENTIF). Moreover, small grafts of mouse epiblast identified mesodermal progenitors able to give to both lateral plate and paraxial mesoderm lineages (Wymeersch 2021). Our findings extend these observations by directly testing the developmental potential of midstreak mesodermal progenitors and demonstrating at the single cell resolution, the versatility of these mesodermal progenitors toward neural, paraxial and lateral plate lineages *in vivo*.

We conducted an analysis of the morphogenetic events that shape the embryo during PS regression. To do this, we combined in toto live imaging with the dynamic Morphoskeleton pipeline [41], which allows projecting tissue dynamics both forward and backward in time. Based on tissue movement identified by PIV analysis, we could identify regions within the developing embryo that act as attractors (towards which cells are converging) such as the primitive streak or repellers (towards which cells are diverging) such as the boundaries between the epiblast fated to give rise to mesoderm and the ectoderm, consistent with known fate maps and dynamics of body axis formation. This validated the use of the morphoskeleton pipeline for the establishment of dynamic fate maps. Through the examination of single cell trajectories in the epiblast, we discovered boundaries that separate domains of different predicted fates with high spatial and temporal resolution. These boundaries form perpendicular to the anteroposterior (AP) axis across the primitive streak (PS) to delimitate the PM, LP, and EEM progenitor domains. The identification of these boundaries and their precise spatial and temporal characteristics is a foundation to generate dynamic fate maps and study the dynamic process of boundary formation and cell fate compartmentalization in remodeling tissues that remain largely unexplored [45,46]. Thus, investigating the mechanisms underlying the establishment and maintenance of these boundaries will provide valuable insights into the complex processes that govern cell fate decisions in vertebrates in vivo.

Next, we utilized direct in ovo gel measurement and live imaging to measure tissue anisotropy over time, to reveal two mechanically distinct tissue environments: tissue remodeling around the node and tissue loss in the posterior domain. We showed that anterior tissue remodeling is dependent on cell division and cell intercalation. This mechanism enables the displacement of daughter cells within the epiblast, allowing them to move in the plane of the tissue and relocate into different progenitor domains. Such a mechanism of cell intercalation upon cell division occurs to dissipate tissue-wide tension generated by PS formation (Firmino, J. et al., 2016, Dev.Cell). Similarly, we observed that during the high remodeling phase, cells move within the epiblast reaching different anteroposterior locations. Once the tissue geometry is established, cell division decreases, and intercalation upon cell division ceases, enabling the establishment of boundaries— or repellers of cell trajectories— which organize cells with similar developmental potential into domains that give rise to distinct preferential fates. These boundaries play a vital role in segregating the different mesodermal territories contributing to cell fate determination during embryogenesis.

Tissue mechanics, compression forces and tissue shearing have become key parameters to influence cell fate in many biological contexts[47]. In our study, we explore the impact of different mechanical environments on epiblast progenitor cell fate decisions by developing a novel method to disrupt tissue movement on one side of the embryo in ovo. Our findings indicate that interfering with the mechanical properties of the epiblast alters the fate of the mesodermal progenitors of the epiblast through altering tissue morphology, SOX2 expression, and cell positions within the epiblast and downstream tissue lineages. Our work highlights the importance of considering tissue dynamics as an additional regulatory factor when studying the gene regulation of SOX2 and potentially other genes involved in cell fate multipotency and determination.

In summary, our study has made substantial contributions to our understanding of developmental plasticity, lineage potential, and the regulation of cell fate decisions by tissue dynamics during embryogenesis. Through the integration of various techniques, including single-cell transcriptome analysis, lineage tracing, tissue dynamics analysis, and perturbation experiments, we have uncovered new insights into the complexity of cell states, the influence of tissue dynamics, and the interplay between intrinsic and extrinsic factors in shaping cell fate. These findings represent significant conceptual advances and enhance our comprehension of the complex processes underlying cell fate decisions in highly dynamic embryonic contexts.

Author contribution:
CG conceptualized and performed most experiments under the supervision of OP. YJ did the single cell analysis and created the new algorithms and associated figures with CG and OP supervision. MS performed the morphoskeleton analysis from movies acquired and tracked by CG. CG, YJ and OP wrote the manuscipt. All authors discussed the data. CG was funded by an EMBO ALTF 406-2015 fellowship, and the project was funded by NIH RO1HD097068-02 to OP. OP supervised the whole project. YD is supplementary orted by Fondation pour la Recherche Médicale (FRM) PLP2020100012456.

Material and methods

Chicken and transgenic quail embryos:

All animal experiments were performed in accordance to all relevant guidelines and regulations. The office for protection from Research Risks (OPRR) has interpreted "live vertebrate animal" to apply to avians (e.g., chick embryos) only after hatching. All of the studies proposed in this project only concern early developmental stages (prior to 5 days of incubation), therefore no IACUC approved protocol is required. Fertilized chicken eggs were obtained from commercial sources. Fertilized eggs from transgenic chickens expressing cytoplasmic GFP ubiquitously were obtained from Susan Chapman at Clemson University. Fertilized eggs from transgenic quails expressing PGK:H2B-mCherry x hUbC:Membrane-GFP were obtained from Rusty Lansford at the University of Southern California. Eggs were incubated at 38 °C in a humidified incubator, and embryos were staged according to Hamburger and Hamilton (HH) or Zacchei stages for chick or quail respectively. We cultured chicken embryos mainly from stage 5HH on a ring of whatman paper on agar plates as described in the EC culture protocol.

Immunohistochemistry:

For whole mount immuno-histochemistry, stage 3 to 20 HH chicken embryos were fixed in 4% paraformaldehyde (PFA)(158127**,** Sigma) diluted in PBS 1X at 4 °C overnight. The embryos were rinsed and permeabilized in PBS-0.1% triton, 3 times 30 min, and incubated in blocking solution (PBS-0.1% triton, 1% donkey serum (D9663, Sigma)) prior to incubating with primary and secondary antibodies. Embryos were incubated in antibodies against T/BRACHYURY (1/1000, R&D Systems: AF2085), SOX2 (1/1000, Millipore: ab5603), PHOSPHO-HISTONE 3 (1/1000, SANTA CRUZ: sc-8656), MSGN1 (1/1000), PHOSPHO-SMAD1 (1/500, Cell Signaling: D5B10) diluted in blocking solution at 4 °C overnight. Embryos were rinsed and washed 3 times 30 minutes in PBS-0.1% triton, incubated 1h in blocking solution and incubated at 4 °C overnight with secondary antibodies conjugated with AlexaFluor (Molecular probes) diluted in blocking solution. If the staining was not imaged in the following 2 days, post fixing was performed using a 4% PFA solution.
Images were captured using a laser scanning confocal microscope with a 10X or 20X objective (LSM 780 or 980, Zeiss). To image the whole embryo, we used the tiling and stitching function of the microscope (5 by 2 matrix) and z sectioning (5um). Later stages (from 17 HH) were imaged in clearing solution using the scale A2 clearing protocol (4 M urea 0.1% Triton, 10% glycerol). For imaging, the embryo was placed in the clearing solution 30 minutes prior to imaging in glass bottom dishes (Mattek).

Plasmid preparation, *in ovo* electroporation for in vivo long-term tracing: *in ovo* electroporation: Chicken embryos at stage 5HH or 8^{-}HH were prepared for in ovo electroporation. Eggs were windowed and a DNA solution (1µg/µl) mixed in HBBS, 30% glucose and 0.1% Fast-green was microinjected in the egg, in the space between the vitelline membrane and the epiblast at the 50% streak between the B1 and B2 boundaries at LP progenitors domain. Electroporation was carried out using 2 pulses at 5V for 1msec on each side of the PS in the LP domains using a needle electrode (CUY614, Nepa Gene, Japan) and an ECM 830 electroporator (BTX Harvard Apparatus). This procedure only labels the superficial epiblast layer. Eggs were then re-incubated for further development.

Nucbow cell tracing: Lineage tracing was performed by co-electroporating *in ovo* as described above the following constructs: a self-excising Cre recombinase (se-Cre), the nucbow construct and the TolII transposase as described in (Loulier et al., 2014) in a 1/1/1 ratio at (1µg/µl, each). We used similar concentrations for the nucbow and transposase plasmids to that described in (Loulier et al., 2014) but increased 10 times the concentration (1 µg/µl versus 0.1 µg/µl) of the se-Cre to favor fast recombination and integration. Because non-integrated nucbow plasmids can remain episomal and transiently affect the color of a cell, we performed our analyses after 36 h when the plasmids are expected to have fully diluted through cell division. 36 h after electroporation, we see that the number of fluorescent cells has significantly decreased suggesting that the episomal transgenes have now been diluted. To perform lineage analysis, we fixed the electroporated embryos at stage 17HH, and imaged them in clearing solution ScaleA2. The imaging was performed using an LSM 880 with Airyscan module in the 3 fluorescent channels using the recommended gating of Loulier et al., 2014)

Quantification: Cells were manually segmented in the YFP and Cherry channel using image J. Positions were assigned to the mesodermal and neural tube layers. Color retrieval was performed by measuring the intensity in the 3 channels, Cerulean, YFP and Cherry so that the total of all the intensities was normalized to 1 and expressed in percentages similarly to Loulier et al., 2014). Cluster assignment was performed using K-mean clustering followed by thresholding of

only the cells with a silhouette >0.4. The coordinates were then calculated in a triplot diagram for visualization. Cells wthin the same space in the triplot have the same color coding.

Labeling and quantification for morphometric analysis:
Nuclear red labelling in ovo : The nuclear red solution was prepared from the NucRed™ Live 647 ReadyProbes™ Reagent (Thermofisher) and diluted in PBS1X as indicated by the manufacturer experimental procedures. Sparse nuclear labelling of the dorsal epiblast was performed *in ovo* by injecting the nuclear red solution between the epiblast and the vitelline membrane at the PS level for 15 minutes. The embryos were then dissected, rinsed in PBS and mounted on paper filter for EC culture to perform live imaging from the dorsal side for the long-term epiblast tracking.
PIV analysis: Whole epiblast of GFP-positive embryo was analysed by computing the velocity field using a custom version of the MATLAB PIV lab software.
Cell tracking analysis: Whole epiblast cell tracking was performed using the plugin from Image J. Tracks were then visualized and analyzed using a custom code in Python. Cell velocities were computed by calculating the discrete displacements. In order to back-track cells in regions of interest, groups of cells were selected at any given time using selection tools provided by the Scikit-image package. Trajectories were then plotted using the Matplotlib package.
Dynamic Morphoskeletons: Given a planar velocity field v(x, t), we identify the Dynamic Morphoskeleton (DM)—i.e. attractors and repellers of cell motion as well as deformation maps--, from the backward and the forward Finite-Time Lyapunov Exponents (FTLE) .
Repellers and deformation analysis: extended material and methods in ([41]

Single cell RNA sequencing preparation and analysis:
Preparation of single-cell suspensions for scRNA-seq: Single-cell dissociation protocols were optimized to achieve >90% viability and minimize doublets before sample collection. To generate the samples, 4 embryos were harvested for each stage and cells were dissociated and captured on an inDrops setup on the same day. Stage 4HH and 3 somites were added to our previous dataset including stage 5HH and 6-somite and 35 somites (Guillot C et al, 2021). For the new samples, we dissected 2 anterior half of the PS including the Hensen's Node and the posterior region of the neural plate and 2 larger regions comprising the PS and adjacent epiblast. For single cell dissociation, the dissected tissue was briefly rinsed in cold PBS, and incubated in Accutase (Gibco) for 10 min at 37 °C followed by mechanical dissociation. The cell suspension was analyzed with a hemocytometer to assess the quality of the dissociation and evaluate cell density. Dissociated cells were centrifuged at 350*g* for 5 min at 4 °C and resuspended at a concentration of 250,000 cells per microliter in 0.25% BSA in PBS. 2× 3,000 cells were sequenced per sample. Two biological replicates were collected per sample and the sequencing data from both samples were combined for data analysis.
Barcoding, sequencing and mapping of single-cell transcriptomes: Single-cell transcriptomes were barcoded using the inDrops pipeline using V3 sequencing adapters as previously reported. Following within-droplet reverse transcription, emulsions consisting of about 3000 cells were broken, frozen at −80 °C, and prepared as individual RNA-seq libraries. inDrops libraries were sequenced on an Illumina NextSeq 500 using the NextSeq 75 High Output Kits using standard Illumina sequencing primers and 61 cycles for read 1 and 14 cycles for read 2, 8 cycles each for index read 1 and index read 2. Raw sequencing data (FASTQ files) were processed using the inDrops.py bioinformatics pipeline available at https://github.com/indrops/indrops. Transcriptome

libraries were mapped to *Gallus gallus* transcriptome built from the GRCg6a (GCA_000002315.5) genome assembly. Bowtie version 1.1.1 was used with parameter –e 200.

Processing of scRNA-seq data: Single-cell counts matrices were processed and analyzed using ScanPy (1.4.3) and custom Python scripts (Code Availability). Low-complexity cell barcodes, which can arise from droplets that lack a cell but contain background RNA, were filtered in two ways. First, inDrops data were initially filtered to only include transcript counts originating from abundantly sampled cell barcodes. This determination was performed by inspecting a weighted histogram of unique molecular identifier–gene pair counts for each cell barcode, and manually thresholding to include the largest mode of the distribution. Second, low-complexity transcriptomes were filtered out by excluding cell barcodes associated with <400 expressed genes. Transcript unique molecular identifier counts for each biological sample were then reported as a transcript × cell table, adjusted by a total-count normalization, log-normalized, and scaled to unit variance and zero mean. Unless otherwise noted, each dataset was subset to the 1,000 most highly variable genes, as determined by a bin-normalized overdispersion metric.

Low-dimensional embedding and clustering: Processed single-cell data were projected into a 50-dimensional PCA subspace, (k = 10 except 35 somite k=15) nearest-neighbor graph using Euclidean distance and 50 PCA dimensions and visualized using UMAP (Uniform Manifold Approximation and Projection) representation. Clustering was performed using Louvain community detection algorithms.

Identification of differentially expressed genes: Transcripts with significant cluster-specific enrichment were identified by t-test comparing cells of each cluster to cells from all other clusters in the same dataset. Genes were considered differentially expressed if they met the following criteria: log-transformed fold change > 0, adjusted P value < 0.05. False discovery rate (FDR) correction for multiple hypothesis testing was performed as described, by Benjamini–Hochberg. The differentially expressed genes, ranked by FDR-adjusted P values, associated fold changes, and sample sizes (number of cells per cluster) are reported in Extended data Table1.

*Opiticlust :*Defined boundaries between cell types among a dataset is essential to create hypothesis about cluster to cluster transitions using optimal transport. We develop an unbiased clustering method allowing the optimal clustering of our cell types. This method considers the significance of the genetic profile of each identified cell population available in our scRNA sequencing data, we called it Opticlust. This program, was created to find the optimal cluster resolution possible according to the significance of every genes for each clusters. OptiClust starts by defining clusters at the lowest resolution possible and increase the resolution number by a pre-defined step until 2 clusters are defined using leiden. Once 2 clusters are defined, for a given clustering resolution, the program check the highest adjusted p-value of the top 1 DEG sorted by score for each clusters. OptiClust consciously increase the resolution at every passage by the pre-defined step until it reach the highest clustering resolution value where the adjusted p-value of one of the first top genes of one of the clusters is inferior to 0.05. Adjusted p-value was obtained using wilcoxon with benjamini-hochberg correction method. This resolution called “optimal value” is then stored in the adata and returned to the user. A visualization tool is also provided in the form of a python widget to automatically display the given resolution and the DEG for every clusters (all the computed leiden resolutions and DEG are also stored and instantly available for the user). Opticlust also include other parameters for fine tuning : position of the gene that needs to be significant in the ranked gene list, resolution range and incremental steps that needs to be tested, p-value adjusted to test, tie-correction and correction-method.

*CADOT :*We developed a tool : Cluster ADJusted Optimal Transport (CADOT) that use probability vectors for every cells to be on the trajectory of a specific clusters at the last timepoint of a multi-timepoint dataset (with at least 3 timepoints) and transition matrices inside a dataset to display the transitions from clusters to clusters between every timepoints. The probability values and the transitions matrices are obtained using Waddington-OT 1.0.7 conceptual framework (Schiebinger et al., 2019). WOT allow us to infer the temporal couplings of cells from the different samples collected independently at various timepoints and get transport matrices. Every timepoints are subsampled to contain to contain the same number of randomly selected cells. Transport matrices (also called 'transport maps') are created by connecting each pair of timepoints and using an estimate of cellular growth rates (to estimate the growth rate, each cell are scored according to its expression of various gene signatures like proliferation and apoptosis as described in Schiebinger et al., 2019 and then model cellular growth with a Birth-Death Process, which assigns each cell a rate of division and a rate of death). Trajectory refers to the sequence of ancestor distributions at earlier time points and descendant distributions at later time points of a cell set C. In the case of CADOT, ancestors probability were used and calculated by pushing back through the transport map. Transition matrices are calculated to show the amount of mass transported from a cell type to another from a start and an end point. The following WOT parameters are used : $\varepsilon = 0.05$ (controls the degree of entropy in the transport map), $\lambda 1 = 1$ and $\lambda 2 = 50$ (A smaller value of $\lambda 1$ or larger value of $\lambda 2$ enforces the constraints less strictly, which is useful when we do not have precise information about the growth rate). CADOT require the usage of a clustering technique to define cell populations and calculate means and standard deviations of probabilities among cells from the same clusters (Given a set C of cells at time j, we use the probability to be an ancestors of C at an earlier time point $i < j$). Then, confidence intervals can be calculated for every clusters and the lowest confidence interval value for every cluster transitions are attributed to every cluster to correct the mean probability (this allow us to correct clusters with small numbers of outliers cells). Filtering clusters probabilities and the transition matrix by user-defined quantiles allow us to visualize the different transitions according to their levels of probability and filter background noise. The result was summarized in a directed data frame containing clusters as node, transitions as edges, probability of transition as edge colors and mass transported as edge sizes. A scanpy compatible python package, containing a WOT wrapper and CADOT computation and visualization functions is available.

Epiblast Grafting

Donor GFP-positive embryos were isolated using the filter method in HBSS and placed on a dissecting plate with a black background. The donor embryo was turned ventral side up, endodermal and mesodermal layers were peeled away and a piece of epiblast (~20 to 50 cells) was cut out using home-made scalpels. Each epiblast piece was checked to ensure that no mesodermal/endodermal cells remained attached before grafting to the best of our ability. A slit in the non-GFP host at the desired location was made to place the donor epiblast. For Lateral plate domain grafts, the epiblast was taken at the 50% mark of the Primitive streak, while the NMP grafts were taken from the epiblast right below the node. We usually took an NMP and an LP epiblast graft from the same GFP donor embryo. Upon regrafting, we removed the excess HBSS and checked that the graft was well inserted into the desired region before putting the embryos back into the incubator for further development on plate culture media. In the majority of cases, the initial graft was cut asymmetrically to ensure proper Antero-Posterior positioning upon regrafting. No differences between asymmetrical and non-asymmetrical grafts were observed

indicating that Antero-Posterior direction did not affect the graft results within such tiny epiblast pieces.

Surgeries for Gel Implants and Quantification:

Stage HH5 GFP-positive embryos were used for surgery experiments. Surgeries were performed *in ovo* under a Leica M90 dissecting scope using a NIGHTSEA GFP lamp in a homemade incubation chamber. Cutting was performed with a homemade scalpel from the dorsal side. The vitelline membrane over the surgery site was first slit in the middle and gently peeled on either side to make a triangular shape opening. Square regions were removed in the dorsal epiblast in the 90% or 50% PS regions. For gel implant, the cleared cut opening received an injection of 1% (w/v) alginic acid sodium (Sigma Aldrich) solution. Injected alginic solution formed gel with calcium ion in the embryo culture and integrated much better than transplant of pre-formed gel. The eggs were then re-incubated and pictures were taken every hour using a zeiss axiocam MRC camera. Here, note that the cut was made only in the epiblast to make sure that the gel stays on top of the endodermal layers. In the case that the endoderm was also cut, the gel sinks into the yolk and the embryo was discarded. To quantify the evolution of the gel implants, we used the Image J software to draw the contour of the graft at different times and retrieve the area. We also measure the Antero-Posterior and medio-lateral length of the gel. We then plot the evolution of the area and the axes over time using Excel software by normalizing to the initial size.

Surgery for filter experiment to hamper tissue flow:

Stage HH8 embryos were used for filter surgery experiments. Surgeries were performed *in ovo* under a Leica M90 dissecting scope in a homemade incubation chamber. A first ring of Whatman paper was placed on top of the vitelline membrane with the embryo in its center and not covered by the filter. The vitelline membrane over the surgery site was first slit in the middle and gently peeled to uncover the embryo. A second rectangular-shaped Whatman filter was placed parallel to the Anteroposterior axis along the PS on the right side. The eggs were then re-incubated for 6 or 12h and pictures were taken at the beginning of the experiment using a zeiss axiocam MRC camera. Following filter surgery, part of the embryos were electroporated with H2B::GFP plasmid at the 50% PS using 1 pulse on each side of the PS and a 100um needle electrode. At the end of the incubation, the embryos were retrieved, fixed, and immunostained using the standard methods explained above.

Using GFP-positive embryos, an video recording under a Leica M90 dissecting scope with a zeiss axiocam MRC camera piloted by micromanager software and a NIGHTSEA GFP lamp we use a scalpel to cut the embryo and measure the relaxation of the tissue after placing the rectangular filter. The relaxation was measured using the kymograph module of FIJI software image analysis.

A. Binagui-Casas, A. Dias, C. Guillot, V. Metzis and D. Saunders, “Building consensus in neuromesodermal research: Current advances and future biomedical perspectives.”, Current opinion in cell biology, vol. 73 , pp. 133–140, 2021.

Briscoe, J., Small, S., ; Morphogen rules: design principles of gradient-mediated embryo patterning. Development 1 December 2015; 142 (23): 3996–4009.

Ferretti E, Hadjantonakis AK. Mesoderm specification and diversification: from single cells to emergent tissues. Curr Opin Cell Biol. 2019 Dec;61:110-116. doi: 10.1016/j.ceb.2019.07.012. Epub 2019 Aug 30. PMID: 31476530; PMCID: PMC6910985.

Firmino, J., Rocancourt, D., Saadaoui, M., Moreau, C., & Gros, J. (2016). Cell Division Drives Epithelial Cell Rearrangements during Gastrulation in Chick. *Developmental cell*, *36*(3), 249–261. https://doi.org/10.1016/j.devcel.2016.01.007

Fowler JL, Ang LT, Loh KM. A critical look: Challenges in differentiating human pluripotent stem cells into desired cell types and organoids. Wiley Interdiscip Rev Dev Biol. 2020 May;9(3):e368. doi: 10.1002/wdev.368. Epub 2019 Nov 19. PMID: 31746148; PMCID: PMC7397816

Fulton T,Verd B and Steventon B 2022 The unappreciated generative role of cell movements in pattern formation R. Soc. open sci.9211293211293http://doi.org/10.1098/rsos.211293

Hayward, M.-K., Muncie, J.M., Weaver, V.M., Tissue mechanics in stem cell fate, development, and cancer Dev. Cell, 56 (2021), pp. 1833-1847, 10.1016/j.devcel.2021.05.011

Gilbert SF, Barresi MJF: Developmental biology. 2020.

Guibentif,C., Griffiths, J.A.,Imaz-Rosshandler I., Ghazanfar S., Nichols J., Wilson V., Göttgens B., Marioni J.C. Diverse routes toward early somites in the mouse embryo Dev. Cell, 56 (2021), pp. 141-153.e6, 10.1016/j.devcel.2020.11.013

Guillot, C., Djeffal, Y., Michaut, A., Rabe, B. and Pourquie, O., “Dynamics of primitive streak regression controls the fate of neuromesodermal progenitors in the chicken embryo.”, eLife, vol. 10 , 2021.

Loulier K, Livet J (2014) Multiplex cell and lineage tracking with combinatorial labels Neuron 81:505–520.

Piatkowska, Agnieszka & Evans, Susan & Stern, Claudio. (2021). Cellular aspects of somite formation in vertebrates. Cells & Development. 203732. 10.1016/j.cdev.2021.203732.

Pijuan-Sala, B., Griffiths, J.A., Guibentif, C., Hiscock, T.W., Jawaid, W., Calero-Nieto, F.J., Mulas, C., Ibarra-Soria, X., Tyser, R.C.V., Ho, D.L.L., et al. (2019). A single-cell molecular map of mouse gastrulation and early organogenesis. Nature 566, 490–495.

Pinheiro,D, Heisenberg C.P, Zebrafish gastrulation: putting fate in motion

Curr. Top. Dev. Biol., 136 (2020), pp. 343-375, 10.1016/bs.ctdb.2019.10.009

Richard H Row, Amy Pegg, Brian A Kinney, Gist H Farr 3rd, Lisa Maves, Sally Lowell, Valerie Wilson, Benjamin L Martin (2018) BMP and FGF signaling interact to pattern mesoderm by controlling basic helix-loop-helix transcription factor activity eLife 7:e31018https://doi.org/10.7554/eLife.31018

Schiebinger, G., Shu, J., Tabaka, M., Cleary, B., Subramanian, V., Solomon, A., Gould, J., Liu, S., Lin, S., Berube, P., Lee, L., Chen, J., Brumbaugh, J., Rigollet, P., Hochedlinger, K., Jaenisch, R., Regev, A., & Lander, E. S. (2019). Optimal-Transport Analysis of Single-Cell Gene Expression Identifies Developmental Trajectories in Reprogramming. Cell, 176(4), 928–943.e22. https://doi.org/10.1016/j.cell.2019.01.006

Serra, M., Streichan, S., Chuai, M., . Weijer, C.J, Mahadevan, L.,. (2020). **Dynamic morphoskeletons in development** Proc. Natl. Acad. Sci., 117 (21) (2020), pp. 11444-11449201908803

Solnica-Krezel L, Sepich DS. Gastrulation: making and shaping germ layers. Annu Rev Cell Dev Biol. 2012;28:687-717. doi: 10.1146/annurev-cellbio-092910-154043. Epub 2012 Jul 9. PMID: 22804578.

Stern CD (2004) Gastrulation in the chick In: Stern C. D, editors. Gastrulation: From Cells to Embryos. Cold Spring Harbor Laboratory Press. pp. 219–232

VanHorn,S, Morris, S.A., Next-generation lineage tracing and fate mapping to interrogate development Dev Cell, 56 (2021), pp. 7-21

Williams RM, Lukoseviciute M, Sauka-Spengler T, Bronner ME. Single-cell atlas of early chick development reveals gradual segregation of neural crest lineage from the neural plate border during neurulation. Elife. 2022 Jan 28;11:e74464. doi: 10.7554/eLife.74464. PMID: 35088714; PMCID: PMC8798042.

Wolpert L. 2016 Positional information and pattern formation. Curr. Top. Dev.Biol.117, 597–608. (doi:10.1242/jeb.098673)

Wymeersch, F.J., Huang, Y., Blin, G., Cambray, N., Wilkie, R., Wong, F.C., and Wilson, V. (2016). Position-dependent plasticity of distinct progenitor types in the primitive streak. eLife 5, e10042.

Wymeersch FJ, Wilson V, Tsakiridis A: Understanding axial progenitor biology in vivo and in vitro. Development 2021:148.

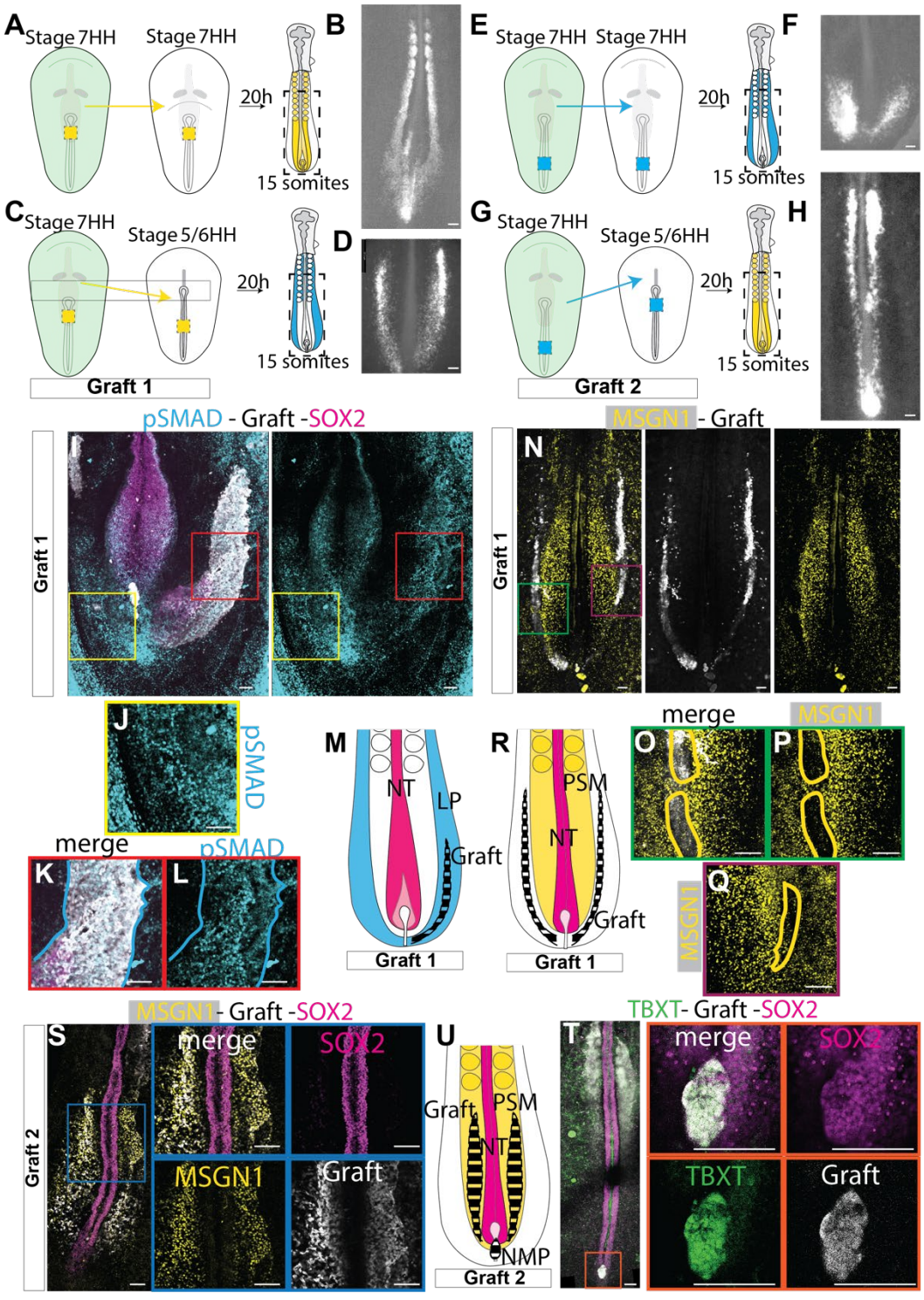

Figure 1: Developmental potency and transcriptional plasticity of epiblast cells of the PS
(A-G) Graft experiments testing the developmental potency of the cells in the predictive LP and NMP progenitors' domains using GFP positive donor and GFP negative hosts.
(A,C) Type 1 graft diagram showing the experimental procedure to graft an NMP progenitor domain of stage 7-8 HH donor into the NMP progenitor domain of stage 7-8 HH host (control, A)

or into the LP progenitor domain of stage 5HH host (experiment, C) and the localization of the GFP positive cells 20h after the graft (B,D).
(E,H) Type 2 graft diagram showing the graft of an LP progenitor domain stage 7-8 HH donor into the LP progenitor domain of stage 7-8 HH host (control, E) or into the NMP progenitor domain of stage 5HH host (experiment, G) and the localization of the GFP positive cells 20h after the graft (F,H).
(I-L) Confocal images of immunostainings on the graft 1 type embryo showing the expression of the LP marker pSMAD1/5/9^{+} (I-M), the paraxial marker MSGN1 (N-Q), the NMP markers SOX2 (I) and the localization of GFP cells 20 h after the graft (white and black line in M,R). Yellow square (I) shows the enlargement of a GFP negative LP region expressing pSMAD1/5/9^{+} (J). Red square (I) shows an enlargement of GFP-positive cells expressing pSMAD1/5/9^{+} (K,L). Green and red squares (N) show the enlargement of GFP-positive cells not expressing MSGN1^{-} (O-Q).
(M,R) Representative diagram showing the localization of the NMP GFP positive cells (black) 20h after the graft into the LP domain. GFP-positive grafted cells are pSMAD1/5/9^{+} (M) and MSGN1^{-} (R) and localize in the lateral plate tissue like LP progenitors.
(S,T) Confocal images of immunostainings on the graft 2 type embryo showing the expression of the paraxial marker MSGN1 (S), the NMP markers TBXT, SOX2 (T), and the localization of GFP cells 20 h after the graft (white or black line in U). Blue square (S) and orange square (T) show the enlargement of GFP-positive cells expressing MSGN1 (S) in the PSM tissue and co-expressing TBXT/SOX2 (T) in the tailbud. (U) Representative diagram showing the localization of the LP GFP positive progenitor cells (black) 20h after the graft into the NMP domain. n>10 embryos.

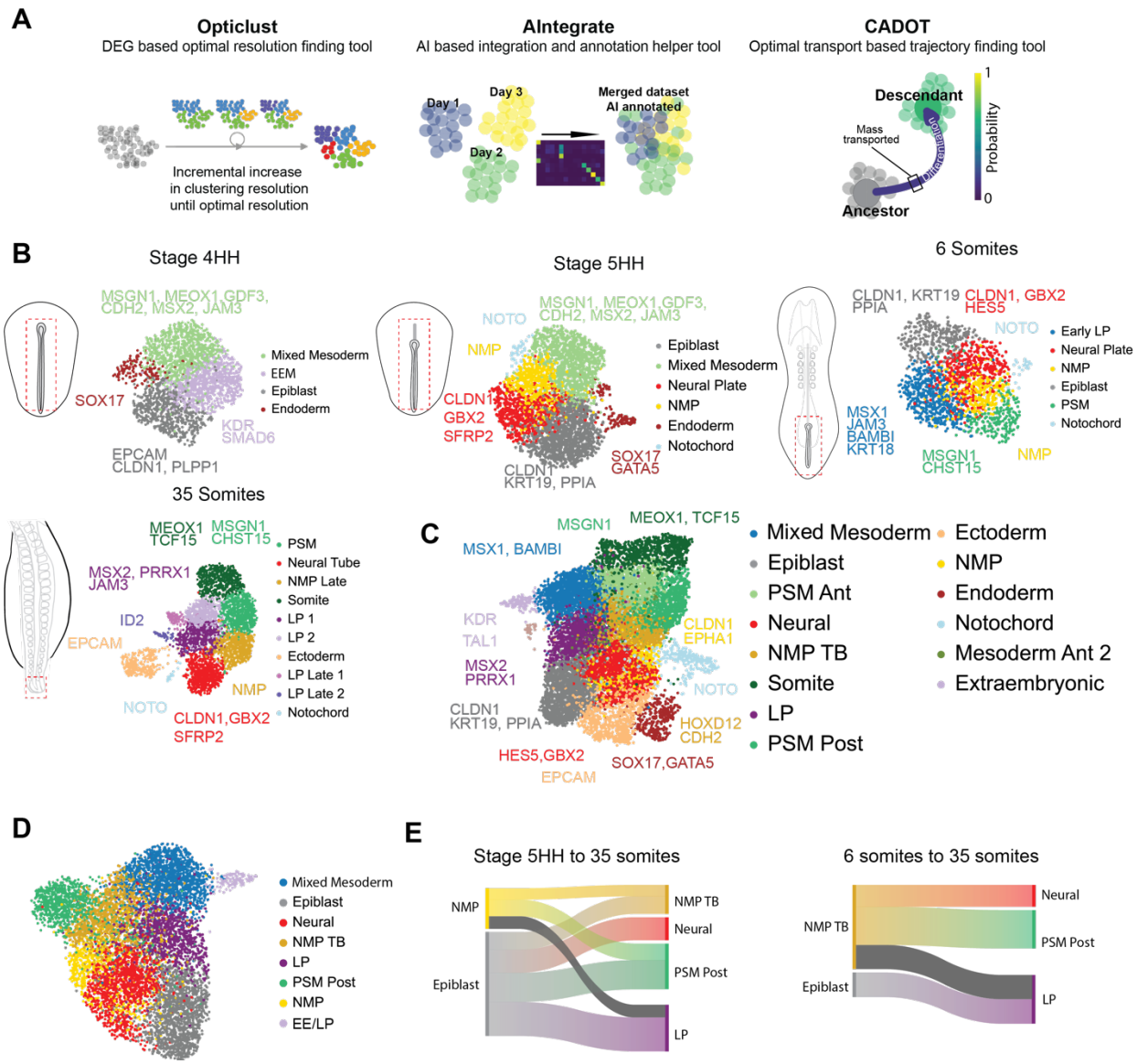

Figure 2 : Generating hypotheses using CADOT and testing them using single-cell lineage tracing to identify the progenitor domains forming the mesodermal lineages.

(A). Trajectory analysis pipeline explained: Each dataset of timepoints is annotated based on the optimal clustering resolution (Opticlust), annotation of integrated datasets is based on a classifier (AIntegrate), and trajectories between every cluster of every dataset is found using optimal transport (CADOT).

(B). UMAP embedding of the single cells from HH4, HH5, 6 somites, 35 somites chicken embryos after bkknn batch correction (50 PC dimensions, 12,000 cells) Colors indicate leiden clustering and cell-type annotations using Opticlust.

(C). UMAP embedding of HH4, HH5, 6 somites, 35 somites chicken embryos merged and processed using bkknn batch correction (50 PC dimensions, 12,000 cells) Colors indicate cell-type annotations of each independent clusters specific to each timepoints, accuracy of annotations was checked using AIntegrate.

(D). UMAP embedding of the clusters of interest (in C) for trajectory analysis (E). Colors indicate cell-type annotations of each independent clusters specific to each timepoints.
(E). Sankey diagram representing transitions from one cell type to another. Transitions within all cell types are computed on two developmental windows from stage 5HH to stage 35 somites (left) and stage 6 somites to stage 35 somites (right). The width of the transitions is proportional to the mass transported. Colors represent cluster colors except for dark transitions representing new lineage predictions. n=3 biological replicates for each stage.

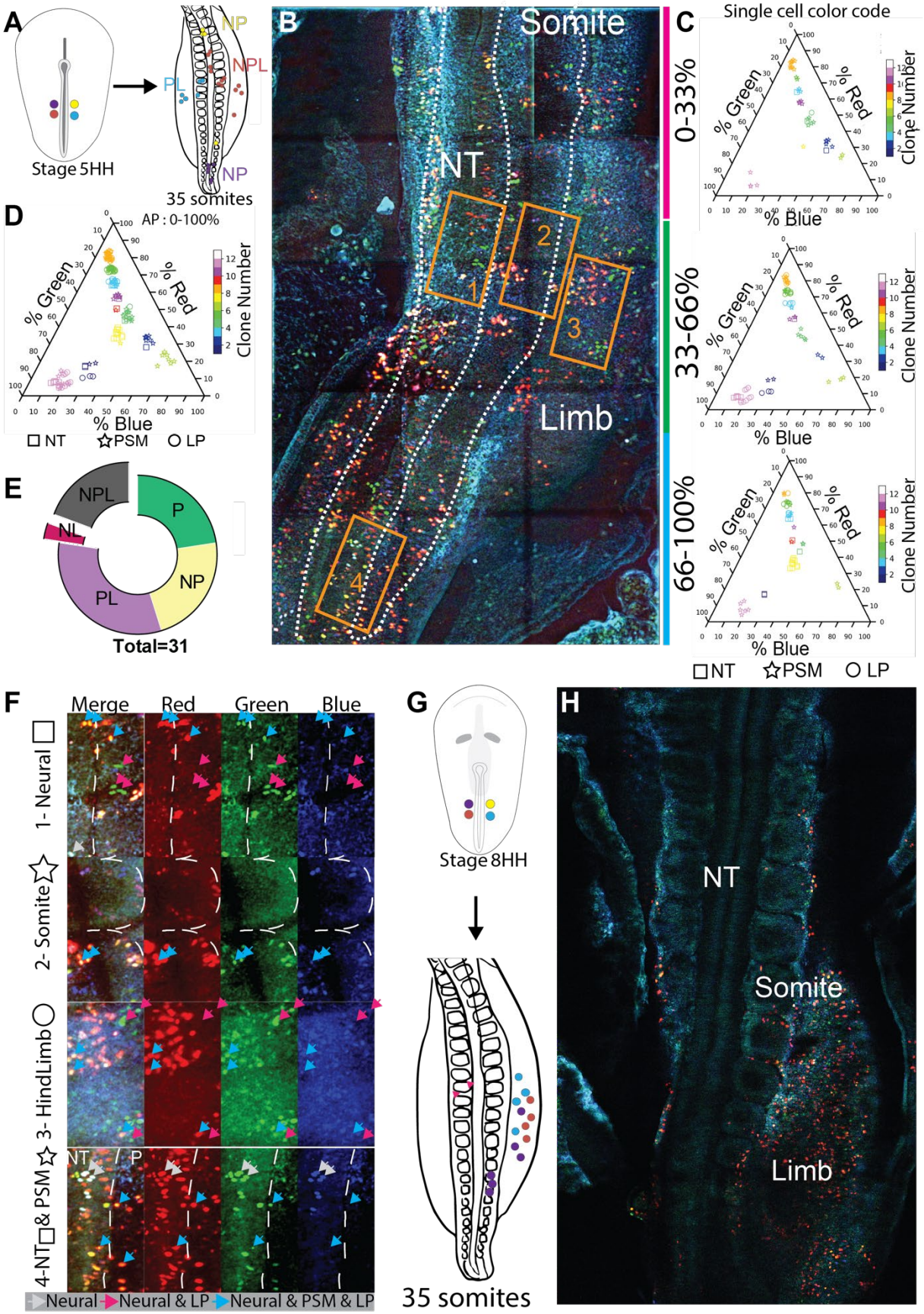
A
Stage 5HH
NP
NPL
PL
NP
35 somites
B
Somite
NT
1
2
3
Limb
4
C
Single cell color code
0-33%
33-66%
66-100%
% Green
% Red
% Blue
Clone Number
NT
PSM
LP
D
AP : 0-100%
% Green
% Red
% Blue
Clone Number
NT
PSM
LP
E
NPL
NL
P
NP
PL
Total=31
F
Merge
Red
Green
Blue
1- Neural
2- Somite
3- HindLimb
4-NT & PSM
NT
P
Neural
Neural & LP
Neural & PSM & LP
G
Stage 8HH
35 somites
H
NT
Somite
Limb

Figure 3 : Single-cell lineage tracing identifies multipotent progenitors in the posterior epiblast domain

(A) Diagram showing the experimental procedure of the electroporated region in the predictive LP progenitor domain of the epiblast at stage 5HH (left) and the stage at which embryos were harvested for analysis (n = 7). Color dots show single cells with a specific color code and their localization at electroporation (left) and at the harvesting time (right). (**B**) Confocal z-projection showing the region of a stage 17HH embryo acquired using three separated laser paths to retrieve the color codes genetically encoded as described in Loulier et al., 2014. (C-D) Triplot diagrams showing the distribution of descendants of cells labeled with different Nucbow combinations along the three different anteroposterior axis (C) or merged (D) of eleven clones in a representative stage 17HH embryo. Each symbol represents a cell identified based on the percentage of red, blue, and green expressed. The symbols are colored based on their clonal identity. Squares: neural cells; stars: paraxial mesodermal cells; circle: lateral plate mesodermal cells. (**E**) Quantification of the different clones: Paraxial mesodermal (P, green) Paraxial and Lateral plate mesodermal (PL, purple), bipotent Neural and Paraxial (NP, gold), bipotent Neural Lateral plate (NL, red) and tripotent Neural Paraxial and Lateral plate (NPL, grey) at stage 17HH (n = 31 clones, in seven embryos). (F) Representative zoom images at different embryo locations drawn in orange in B showing color-coded cells with different fates. Grey arrows show a representative clone of only neural cells with the same color code : 30/30/30 Red/Green/Blue corresponding to the clone 7 yellow (C,D); pink arrows show a representative clone of Neural and Lateral plate mesodermal cells with a color code 10/80/10 Red/Green/Blue, corresponding to the clone 11 purple (C,D) and light blue arrows show cells in the Neural, Paraxial and Lateral plate cells with 65/25/10 Red/green/Blue color code corresponding to the clone 3 light blue (C,D). Square: neural cells, star: PSM cell, Circle: Lateral plate cell. (G) Diagram showing the experimental procedure of the electroporated region of the predictive LP progenitor domain of the epiblast at stage 8HH (top) and the stage at which embryos were harvested for analysis (n = 5). Color dots show single cells with a specific color code and their localization at electroporation (top) and at the harvesting time (bottom). (**H**) Confocal z-section showing the region of a stage 17HH embryo acquired using three separated laser paths to retrieve the color codes genetically encoded.

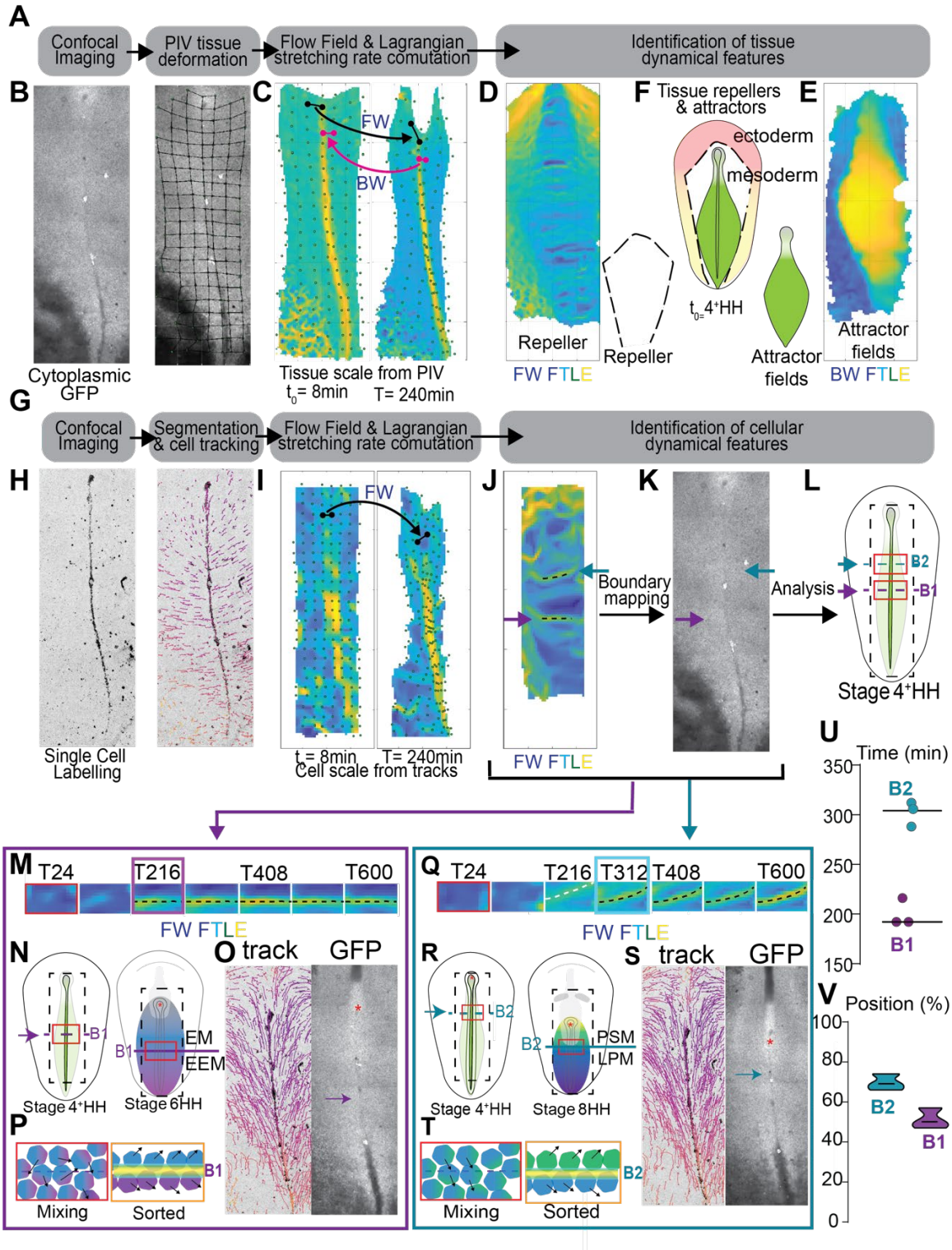

Figure 4 : Analysis of the tissue and cell dynamics identifies boundaries between epiblast territories

(A-E) Workflow (A) to identify repellers and attractors using the dynamic morphoskeleton on tissue-wide deformations. Representative images (B-E) showing the raw confocal image of cytoplasmic GFP embryos (B, left) analyzed with the morphoskeleton to calculate the grid

deformation (B, right) and the flow field (C) used to compute the Forward and Backward FTLE to identify the repellers (D) and attractor flow field (E) organizing the remodeling epiblast as summarized in the diagram (F). (G-V) Workflow (G) to identify repellers and attractors using the dynamic morphoskeleton on cell tracks. Representative images (H-L) showing the raw confocal image of nuclearRed labeled embryos (H, left) analyzed with the morphoskeleton to calculate the grid deformation (H, right) and the flow field (I) used to compute the Forward FTLE to identify the repellers (yellow and black dotted line) (J) organizing the remodeling epiblast and summarized in the raw image (K) and diagram (L). (M,Q) Close-up of the FW FTLE color-coded image showing the dynamic formation of the Boundary 1 (black dotted line, M) and 2 (black dotted line, Q) over time. The white dotted line in Q shows an unstable repeller. (N-O, R-S) Representative diagram showing the localization in space (N,R), the cell trajectories (O,S left), and the raw image (O,S, right) at the time (purple and blue square) of boundary formation. (P,T) Diagrams showing the cell shuffling before the boundary form and cell sorting after the boundary form to form two distinct tissue compartments on each side of the Boundaries. (U,V), Quantification of the time (U) and location (V) of the boundary formation. n=3 embryos.

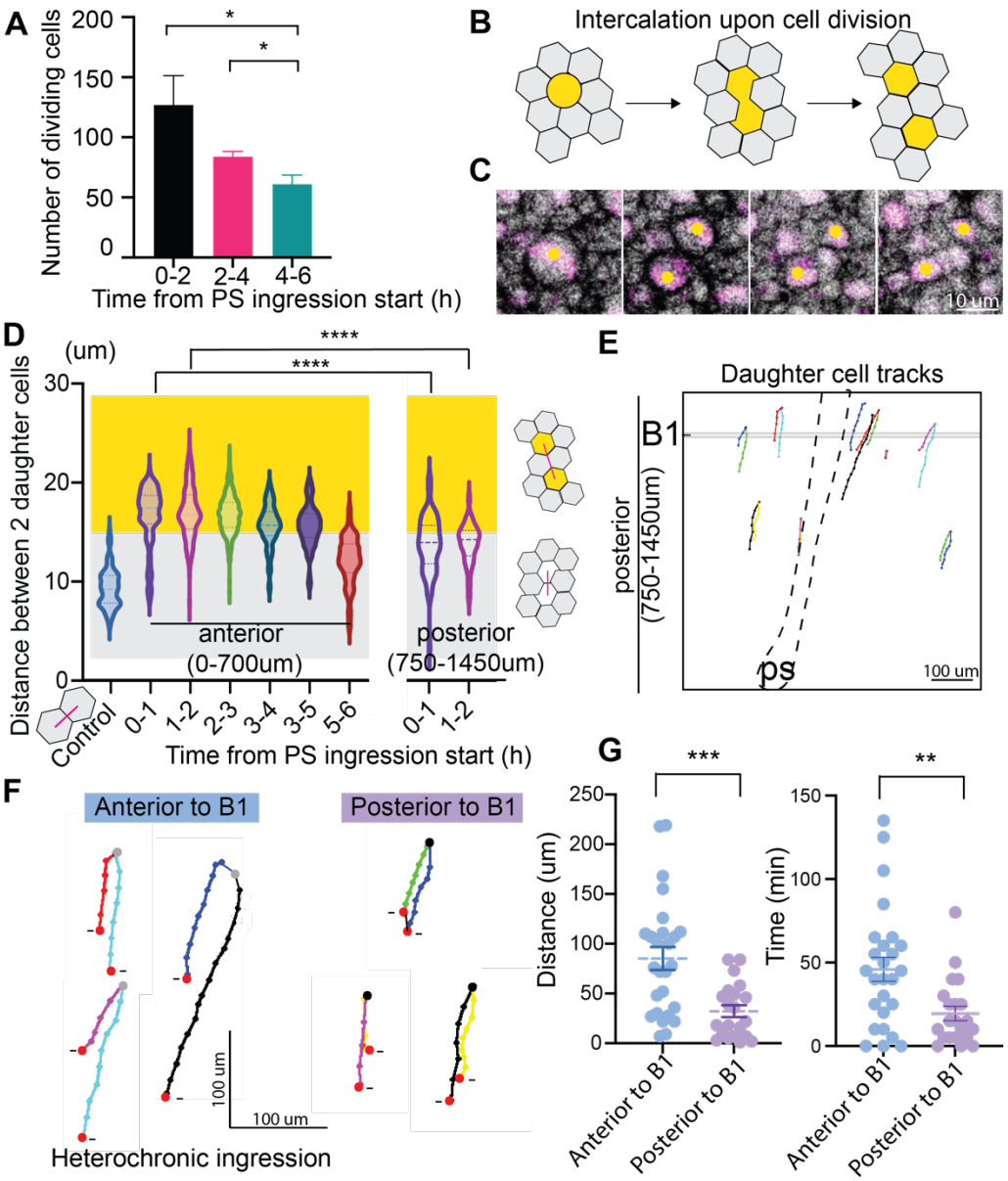

Figure 5: Displacement of epiblast progenitors depends on cell intercalation following cell division

(A) Quantification of the number of dividing cells in the epiblast with a 2-hours binning window from the beginning of PS regression (0hour). (N=2 embryos, n=1109 division events) (B) Diagram showing the process of cell intercalation upon cell division (yellow cell) within the epiblast tissue (grey). (C) Representative image of intercalation upon cell division using transgenic nuclear red and membrane GFP quail embryos. Scale bar = 10 um. (D) Quantification of the distance between cells after they divide in the anterior and posterior PS over time. 0 hours marks the start of PS regression. Distance in the control represents the distance between 2 cells in the epiblast. The

yellow zone shows the data range where measurements are consistent with twice the mean distance between cells in the epiblast (ie: the intercalation of 1 cell). N=2 embryos, n=1149 division events. (E) Representative manual tracking of daughter cells dividing in the posterior PS region (750 to 1450um) where B1 forms (grey) . (F) Single manual tracks of daughter cells after they divide anterior to the B1 location (grey dots, left) or posterior to the boundary region (black dots, right). Red dots show the end of sister cell tracking due to ingression (-). (G) Quantification of the distance (left) and time (right) between the sister cells ingression coordinates for sister cells born anterior (blue) or posterior to B1 location (violet) N=2 embryos, n=47 cells. Scale bars = 100 um.

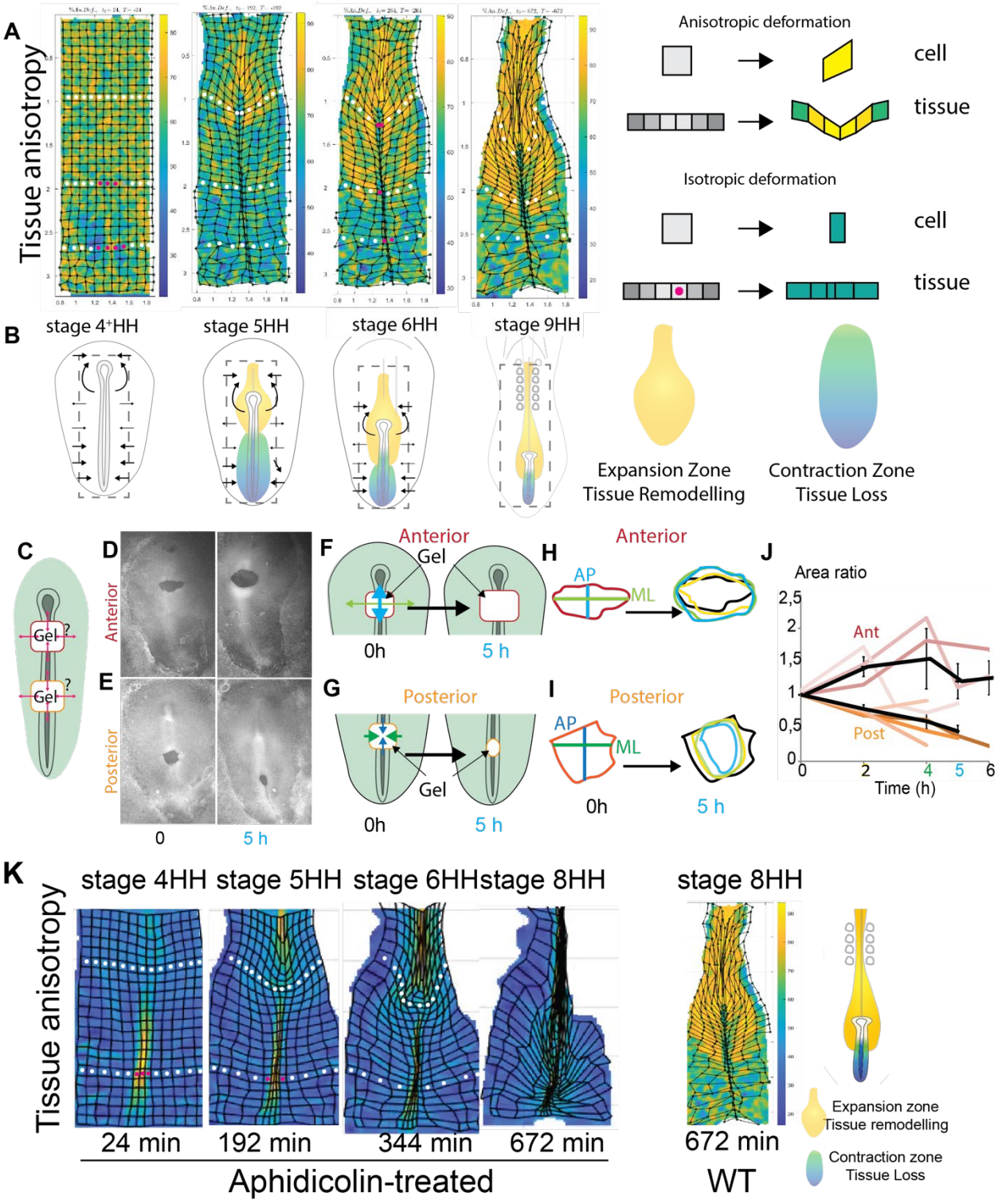

Figure 6: Anterior and posterior epiblast cells are exposed to distinct mechanical constraints. (A-B) Representative images (A) and diagrams (B) from in toto live imaging displaying the percentage of anisotropic tissue deformation (yellow) at increasing time intervals of cytoplasmic GFP embryos highlighting tissue deformations (grid size = 80um) (n=3). White dots show tissue remodeling zones and pink dots show tissue loss regions. (C-G) Diagram (C), representative

images (D,E), enlarged diagram (F,G) of the gel implant shape at t=0h and t=5h after the implantation. (H-L) Morphometric quantifications of the gel implant in the anterior (up) and posterior (down) regions. (H-I) Shapes delimitating the gel implant at t=0h (left) and overlay of the shapes over 5 hours in the anterior (H) and posterior (I) epiblast region. The color coding shows the time after gel implantation 0h, black, 2h yellow, 4h green, 5h blue. AP= Anteroposterior length (Blue), ML= Mediolateral length (green). (J) Quantification of the evolution of the area normalized to its initial gel sizes at t=0h and over 6 hours. Black curve is the mean curve n=8 embryos. (K) Representative images displaying the percentage of anisotropic tissue deformation (yellow) at increasing time intervals using cytoplasmic GFP embryos showing tissue deformations in aphidicolin-treated embryos (left) compared to WT embryos (right) (grid size = 80um) (n=3) White dots show tissue remodeling zones and pink dots show tissue loss regions.

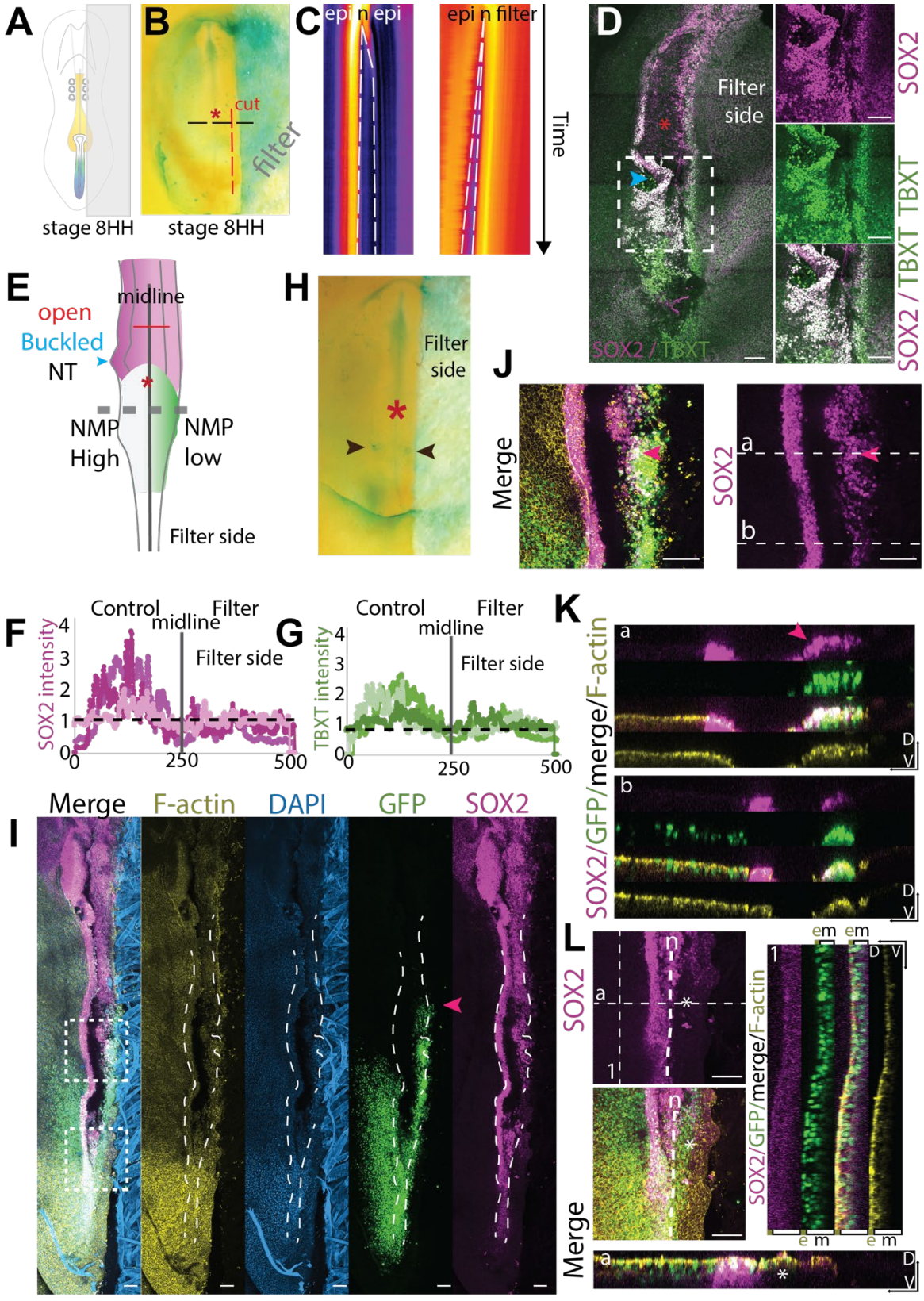

Figure 7: Interfering with epiblast mechanical properties affect the fate of mesoderm progenitors

(A) Diagram and (B) representative image showing filter positioning to interfere with tissue remodeling. The red stippled line shows the location of the cut to test tension changes. The black stippled line shows the position of kymograph tissue analysis. (C) Kymograph showing the opening relaxation after cutting the embryo in WT (left) and embryos with filter (right). (D-G) Representative image (D), diagram (E) and quantifications (F,G) showing the localization of TBXT (green) and SOX2 (purple) in filter embryo that developed overnight. (H) Representative image showing the electroporation sites in the LP domain (arrows). (I-L) Representative images (I) showing the localization of the electroporated cells (green), the F-actin (yellow), DAPI (blue) and SOX2 (purple) in stage 8HH electroporated embryo incubated overnight after placing the filter on the right side. (J-L) Enlarged images of the anterior neural tube (J) and node/primitive streak (L) regions. Dorsal (J) and lateral (K) views at two different axis locations (J a,b) showing the anterior location in the SOX2 positive neural cells of GFP electroporated cells in the filter side (K). We find no GFP positive cells in the $SOX2^{+}$ neural tube in the no filter side while some green cells are in the mesodermal layer. (L) Dorsal (left) and lateral views (1,a) of the node/Primitive streak region showing the loss of SOX2 expression in the filter side (asterisk). We find GFP positive cells in the mesoderm layer laterally in the no filter side all aloing the anteroposterior axis (L, right, 1). Very few GFP positive cells remain in the progenitor region on the filter side. n > 7 embryos.

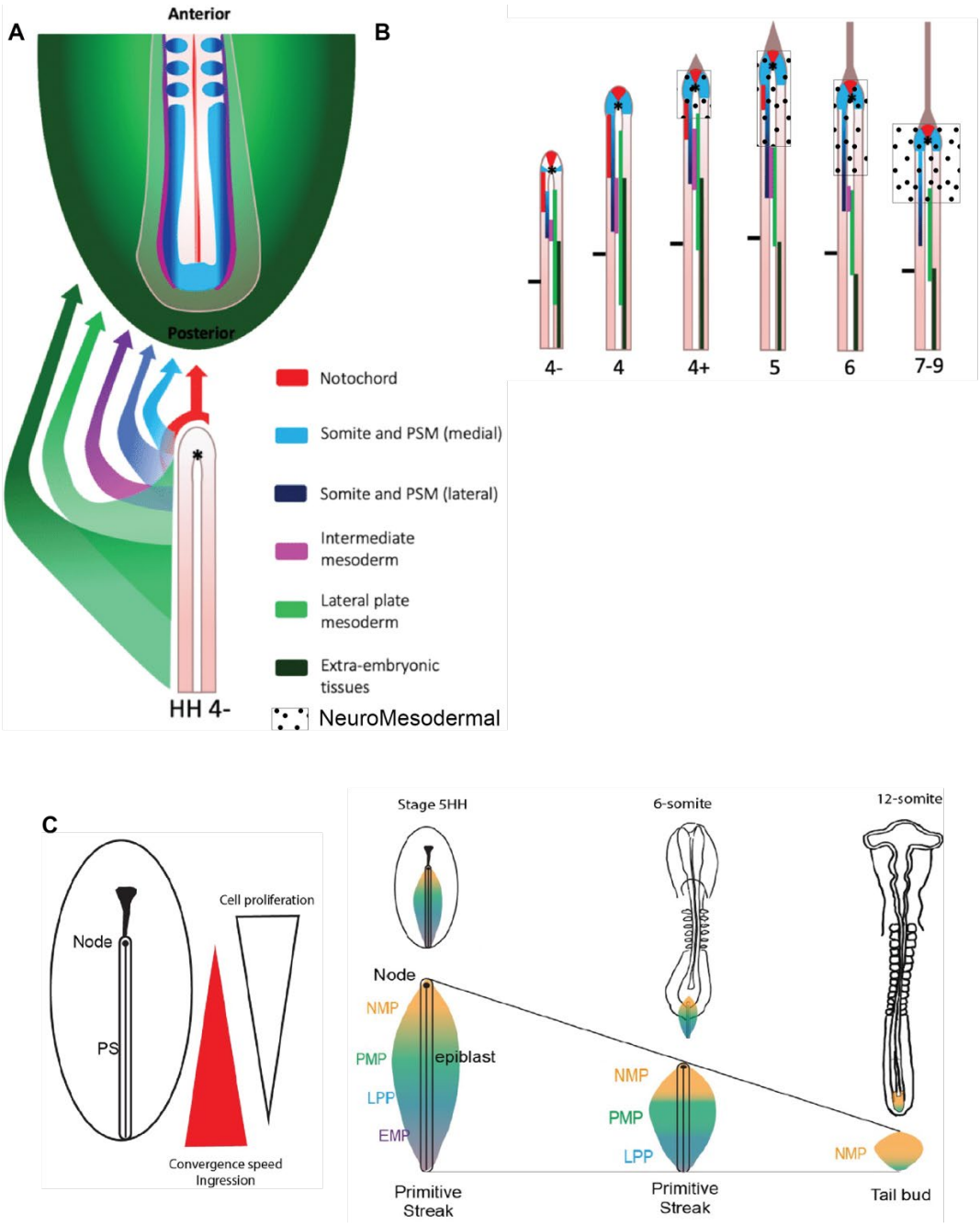

Supplementary Figure 1: Organization of the fate, dynamics, and signaling in the mesodermal plate of chick embryos.

(A,B) Diagram adapted from *Piatkowska, A et al, Cells & Development, 2021* showing the fate map landscape of the mesodermal tissues in the chick embryos (A) and their original localization along the PS from *Psychoyos and Stern, 1996* (B) and the localization of the Neuromesodermal domain (dots). (C) Diagram showing the gradient of cell movements along the PS during mesoderm internalization from *Guillot ,C., et al, eLife, 2021*. NMP : Neuromesodermal, PMP:

Paraxial Mesoderm Progenitors ; LPP: Lateral Plate Progenitors; EMP : Extra Embryonic Progenitors.

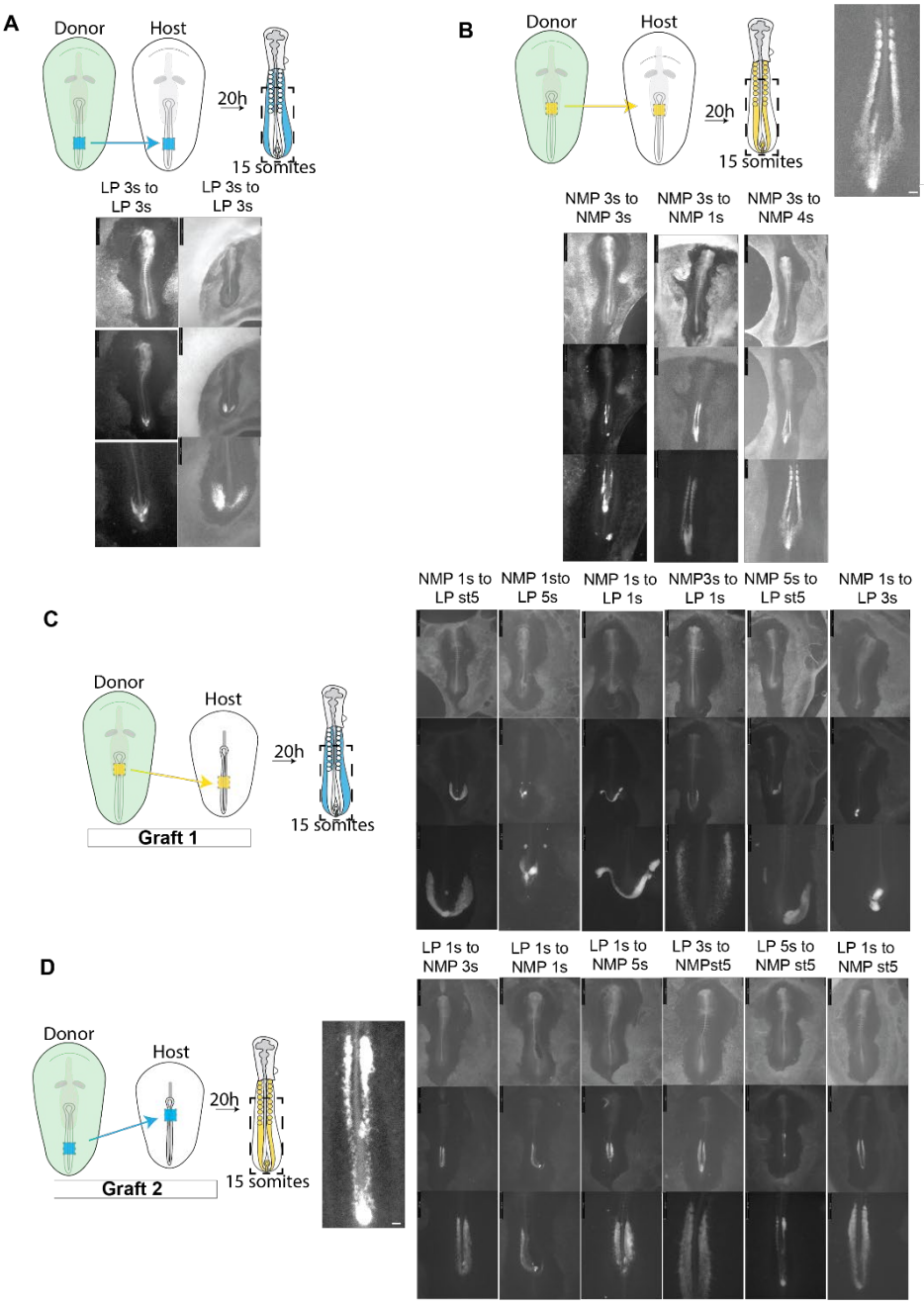

Supplementary Figure 2 : Testing developmental potencies of the post gastrulating epiblast using graft experiment

Graft experiments testing the developmental potency of the cells in the predictive LP (A,D) and NMP (B,C) progenitors' domains using GFP positive donor and GFP negative hosts. (A,C) Type 1 graft diagram showing the experimental procedure to
graft an NMP progenitor domain of stage 7-8 HH donor into the NMP progenitor domain of stage 7-8 HH host (control, A) or into the LP progenitor domain of stage 5HH host or stage 7-8 HH host (experiment, C) and corresponding macroscope pictures showing the localization of the GFP positive cells 20h after the graft (right). (B,D) Type 2 graft diagram showing the graft of an LP progenitor domain stage 7-8 HH donor into the LP progenitor domain of stage 7-8 HH host (control, B) or into the NMP progenitor domain of stage 5HH host or stage 7-8 HH host (experiment, D) and corresponding macroscope pictures showing the localization of the GFP positive cells 20h after the graft (right).

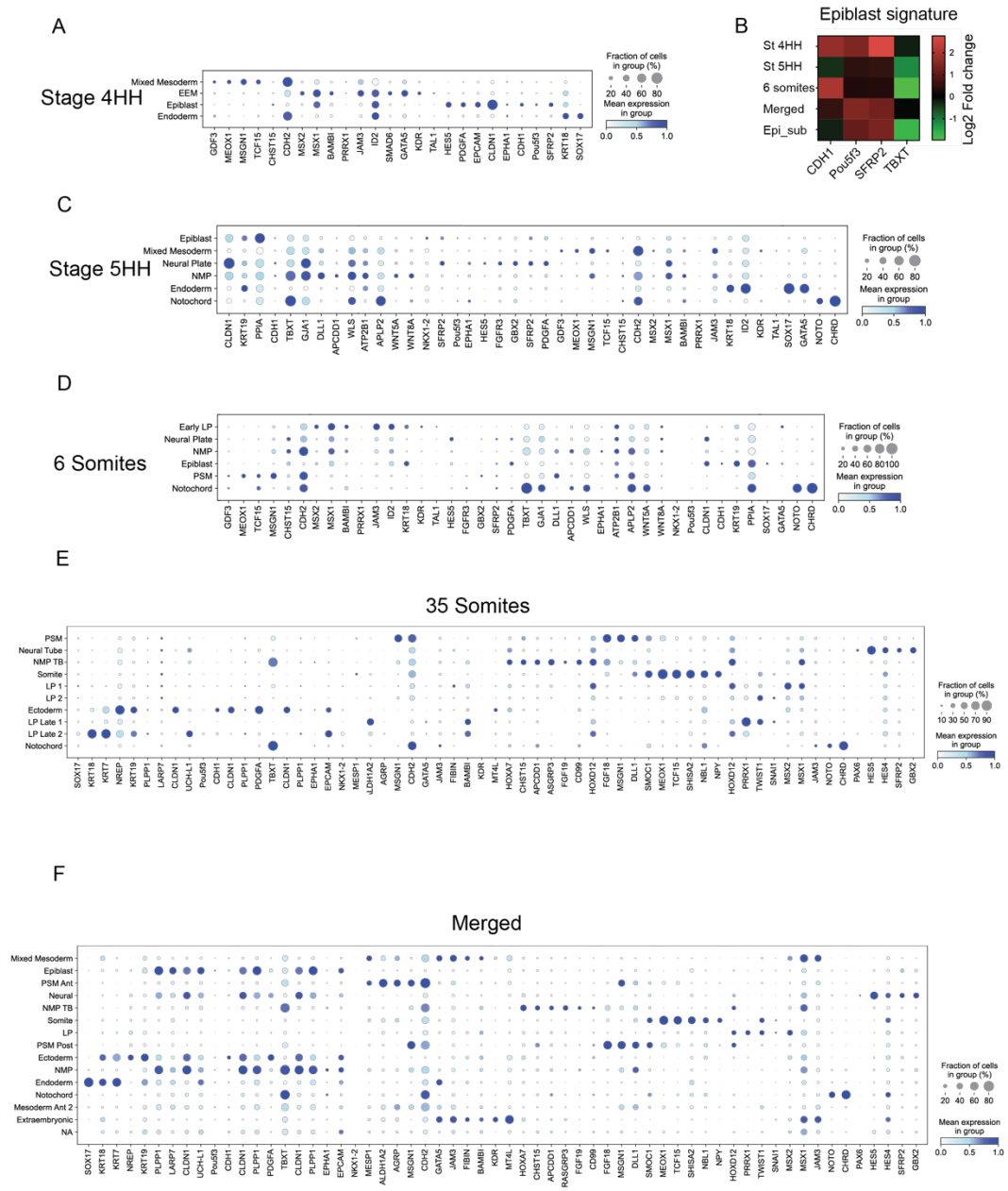

Supplementary Figure 3 : Marker genes expression to analyze the identity of the clusters identified by unsupervised optimal clustering.

Dot plots showing the expression of the marker genes used to identify the cluster identity at stage 4HH (A), stage 5 HH (C), 6 somites (D), 35 somites (E), and all the stages merged (F). (B) Heat map showing the expression in log2 fold change of primed epiblast markers genes in the different epiblast clusters of 4HH, 5HH, 6 somites, merged and subclustered (Figure 2 D) developmental stages.

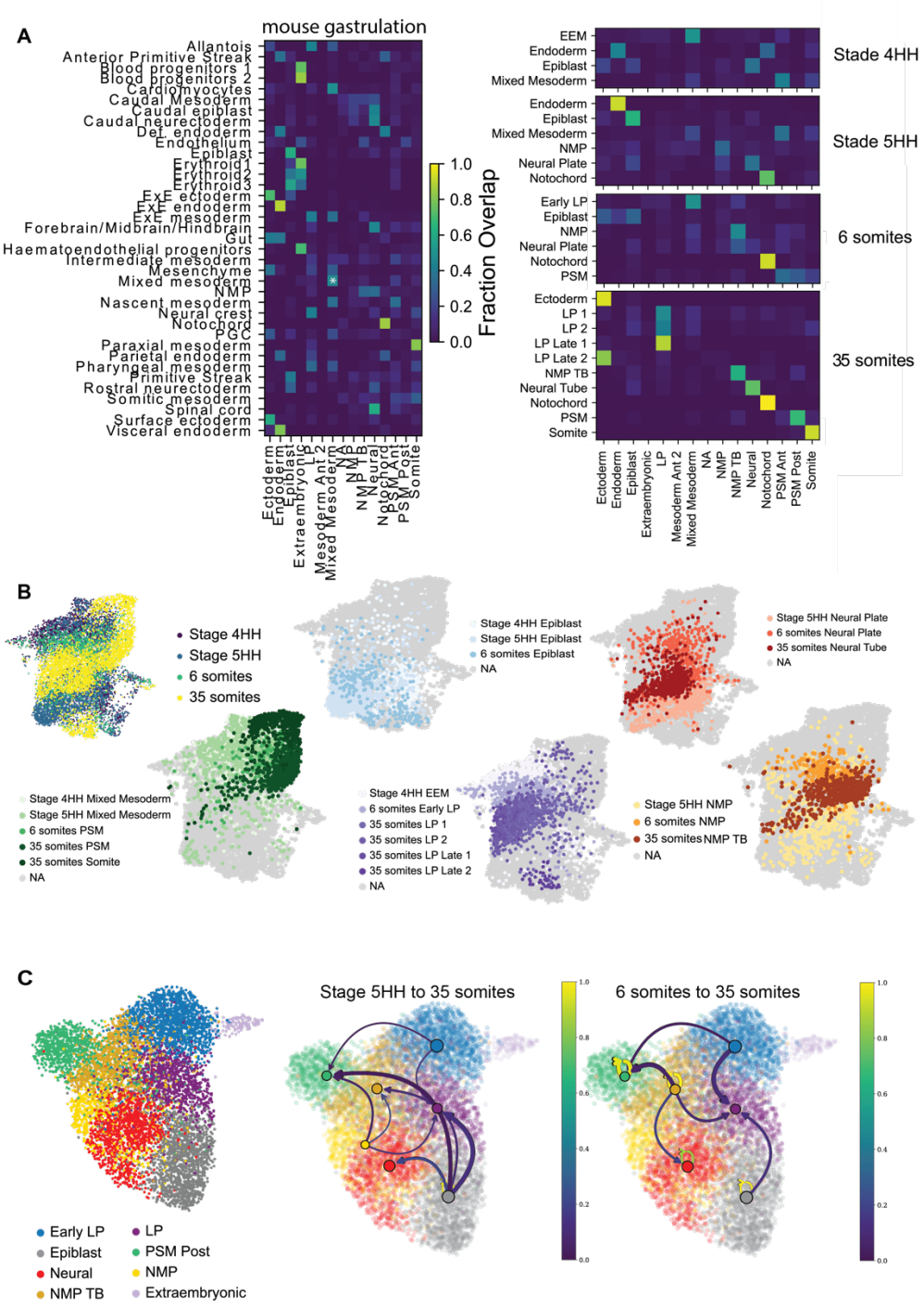

Supplementary Figure 4: CADOT and AIntegrate : trajectory and annotations methods

(A). Aintegrate classifier showing the correlation (fraction overlap) between the merged chicken dataset from this study and the mouse gastrulation clustering from the Pijuan-Sala 2017 study (left). AIntegrate classifier showing the correlation (fraction overlap) between annotations in the integrated and merged dataset containing stage 4HH, 5HH, 6 somites and 35 somites and individual datasets annotated using the opticlust clustering method (right).

(B). UMAP embedding of HH4, HH5, 6 somites, 35 somites chicken embryos merged and processed using bkknn batch correction (50 PC dimensions, 12,000 cells) Colors show the timepoints (upper left image) and the projected space of the cell-type annotations (all other images).
(C). CADOT analysis of cell movement (cluster to cluster transitions) from stage 5hh and 6somites to stage 35 somites. Arrow colors indicate the probability of the transition, arrow size indicates the associated quantity of cells transported from one cluster to another in the merged dataset containing stage 4HH, 5HH, 6 somites, and 35 somites on clusters of interests.

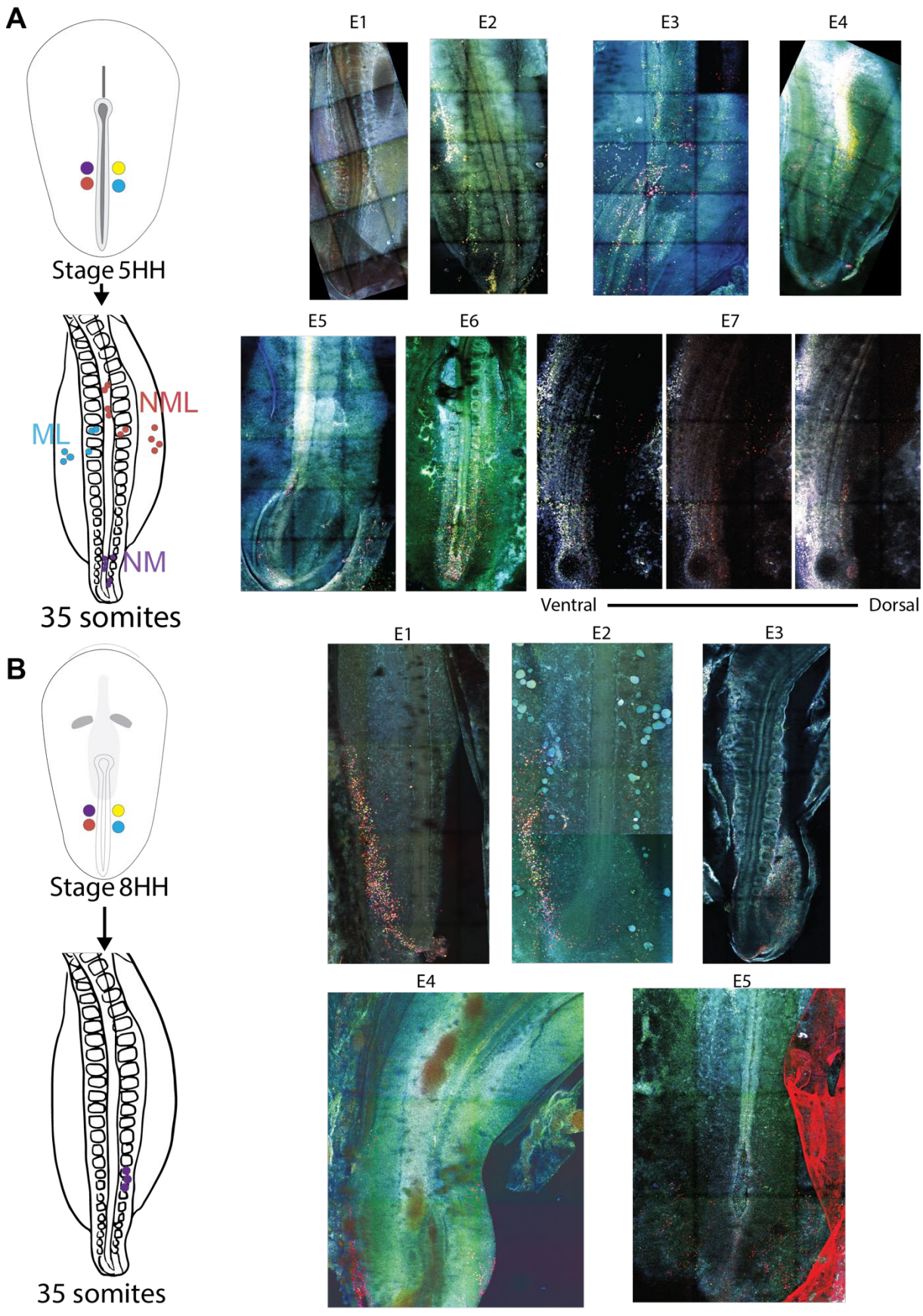
A
Stage 5HH
NML
ML
NM
35 somites
E1
E2
E3
E4
E5
E6
E7
Ventral
Dorsal
B
Stage 8HH
35 somites
E1
E2
E3
E4
E5

<u>Supplementary Figure 5:</u> Single cell lineage tracing of 50% primitive streak cells at stage 5HH and 8HH.

(A). Diagram (left) and projection (right) of confocal images showing embryos at 72h of development after labeling of the 50% primitive streak at stage 5HH.

(B). Diagram (left) and projection (right) of confocal images showing embryos at 72h of development after labeling of the 50% primitive streak at stage 7-8 HH.

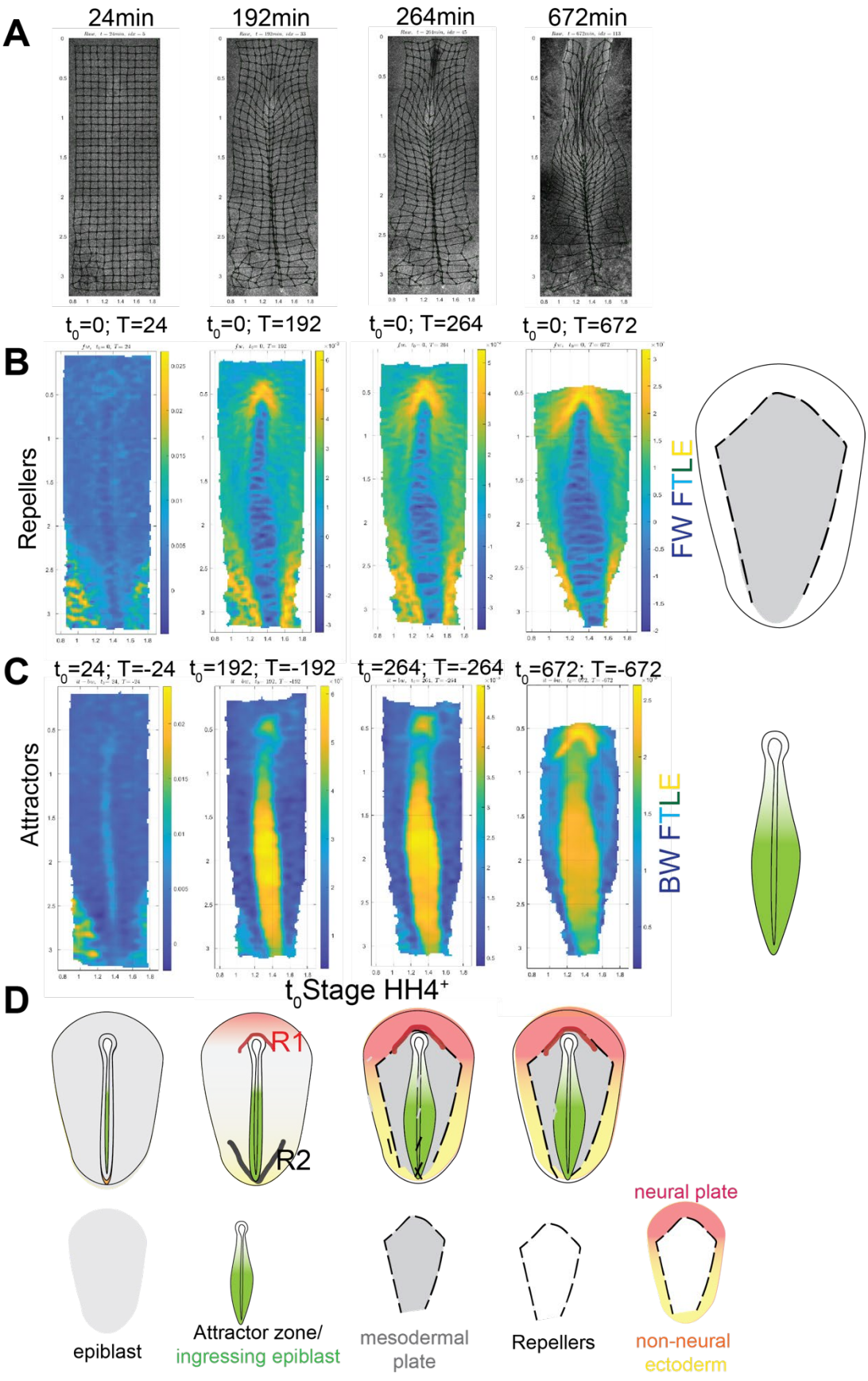
A
24min
192min
264min
672min
B
t_0=0; T=24
t_0=0; T=192
t_0=0; T=264
t_0=0; T=672
Repellers
FW FTLE
C
t_0=24; T=-24
t_0=192; T=-192
t_0=264; T=-264
t_0=672; T=-672
Attractors
BW FTLE
D
t_0Stage HH4+
R1
R2
epiblast
Attractor zone/
ingressing epiblast
mesodermal
plate
Repellers
neural plate
non-neural
ectoderm

<u>Supplementary Figure 6:</u> Analyzing tissue mechanics and remodelling during PS regression doesn't identify distinct progenitor domains within the mesodermal plate.
(A) Raw images of cytoplasmic GFP embryo images for 12 hours from the beginning of PS regression. The over-imposed grid is used to measure tissue anisotropy (grid size 80um). (B-D) Representative images (B-C) and diagrams (D) of the cytoplasmic GFP embryos analyzed with the morphoskeleton showing the repellers (B) and attractors (C) regions that organize the dynamics of PS regression in WT embryos (n=3) and its legend (bottom).

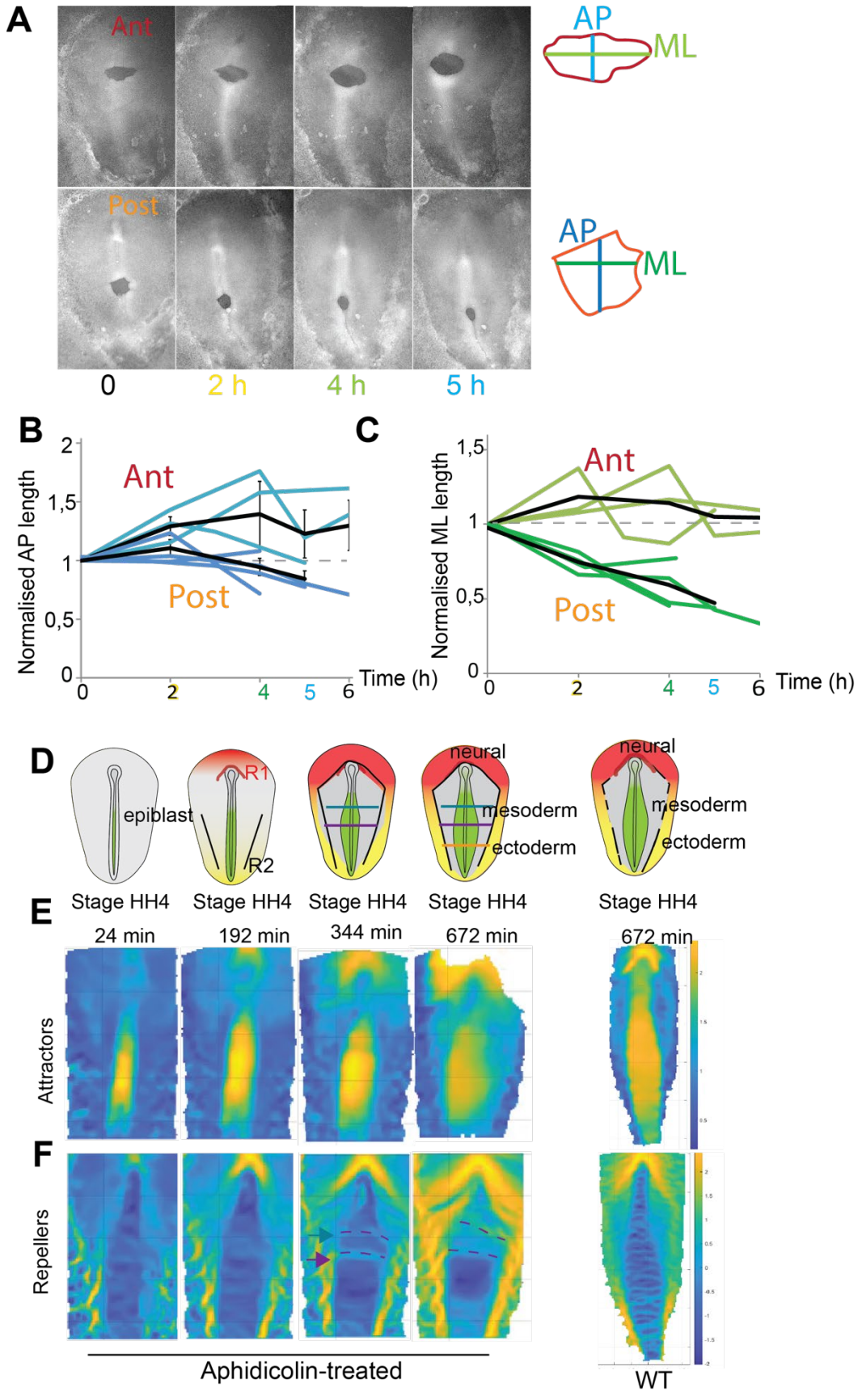
A
Ant
Post
AP
ML
AP
ML
0
2 h
4 h
5 h
B
Ant
Post
Normalised AP length
Time (h)
C
Ant
Post
Normalised ML length
Time (h)
D
epiblast
R1
R2
neural
mesoderm
ectoderm
neural
mesoderm
ectoderm
Stage HH4
Stage HH4
Stage HH4
Stage HH4
Stage HH4
E
24 min
192 min
344 min
672 min
672 min
Attractors
F
Repellers
Aphidicolin-treated
WT

Supplementary Figure 7: Morphoskeleton analysis of in toto live imaging over 8 hours movies in Aphidicolin-treated embryos identifying the repellers and attractors organizing tissue remodelling during PS regression

(A-C) Images (A) and quantifications (B,C) of the anteroposterior (B) and mediolateral (C) normalized length of the gel implant in the anterior (light) and posterior mesodermal plate domains after gel implantation in ovov (t=0) and analyzed every hour for 5 h. (n=8). (D-F) Diagrams (D) and representative images of cytoplasmic GFP embryos analyzed with the morphoskeleton showing the attractors (E) and repellers (F) regions that organize the dynamics of PS regression in aphidicolin-treated embryos (left) compared to WT embryos (right) (n=3).

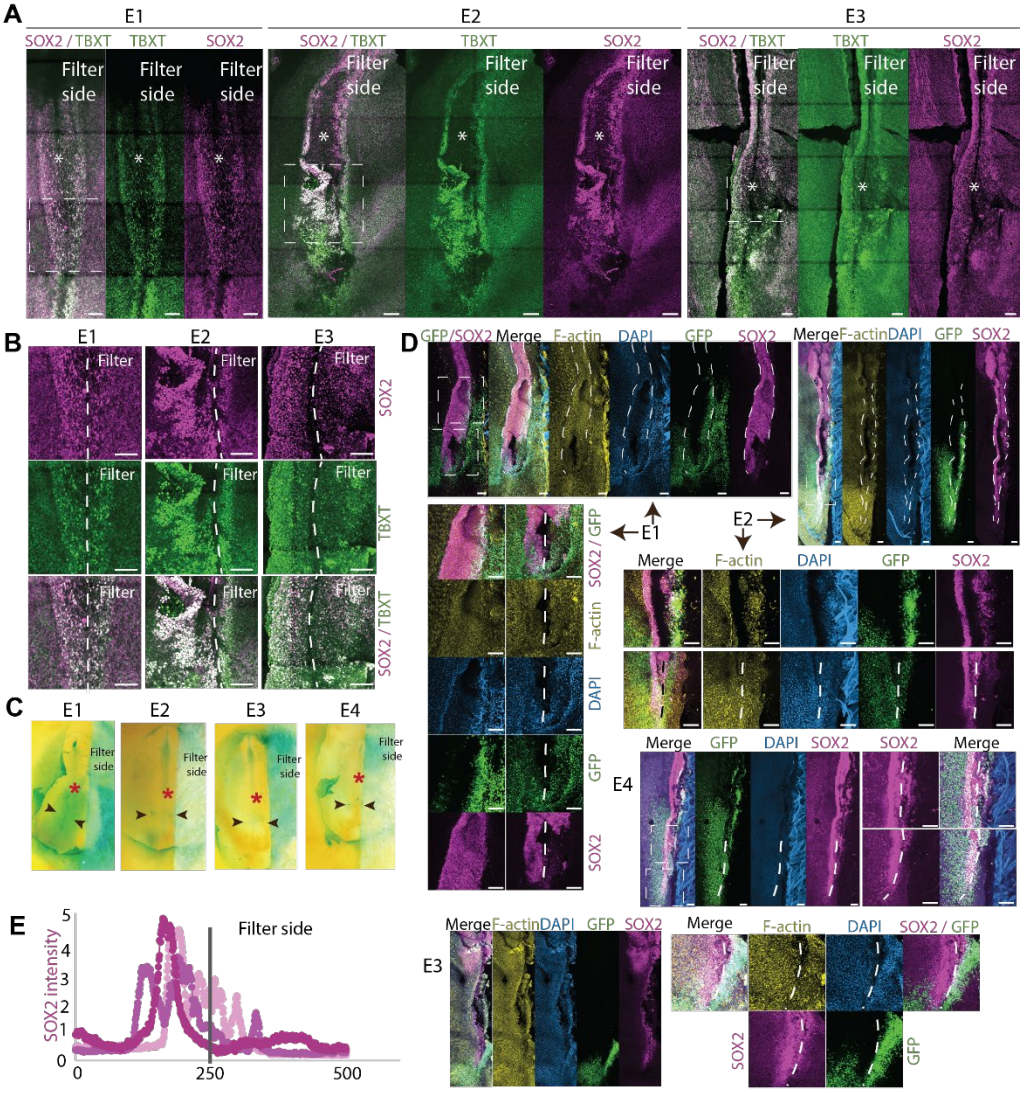

Supplementary Figure 8: Analysis of the NMP markers after hampered tissue tension

(A). Confocal images showing the localization of TBXT/SOX2 in embryos 12h after placing a filter *in ovo* on the right side.

(B). Close up of the dotted square in (A).

(C). *In ovo* images showing the filter positioning and electroporated regions at 50% primitive streak (arrow) and Node region (star) (N=4).
(D). Confocal images showing the localization of GFP/SOX2 cells 24h post-electroporation and immunostained using SOX2 (Neural marker), GFP (electroporated cells), DAPI (all nuclei) and F-actin (cell membrane).
(E). Quantification of SOX2 intensity posterior to the node across the medio-lateral axis, 24h post-filter application in hampered tissue mechanics. Scale bars = 100um.

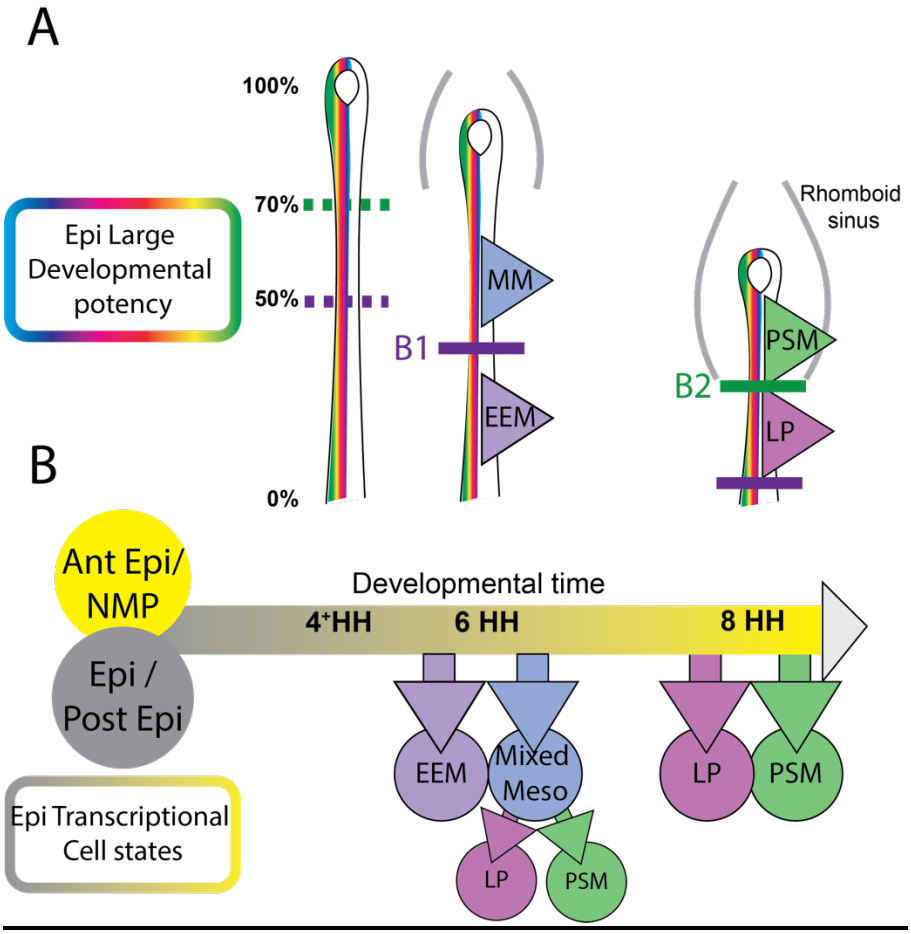

Supplementary Figure 9: Dynamic map analysis of the developmental potency and fate of the epiblast progeniors in the mesodermal plate of chick embryos.

(A) Diagram showing the spatial location of ingression which give rise to distinct mesodermal-fated territories (arrows) from the two epiblast cell states (yellow and grey) with large developmental potency (rainbow). The boundary B1 (purple) and B2 (green) which organize the epiblast progenitors into distinct domains are depicted as a solid line when the boundary form and is stable and as a dotted line to show the tissue location which will be separated when the boundary form. (B) Diagram showing the temporal sequence of mesodermal fate diversification from the

two epiblast cell states (yellow and grey) with large developmental potency (rainbow). MM : Mixed mesoderm, EEM : Extraembryonic mesoderm, LP : Lateral Plate mesoderm, PSM : Paraxial mesoderm. B1, B2 : Boundary 1 and 2.

1. Stern, C.D. (2004). Gastrulation: from cells to embryo (Cold Spring Harbor Laboratory Press).
2. Sheng, G., Martinez Arias, A., and Sutherland, A. (2021). The primitive streak and cellular principles of building an amniote body through gastrulation. Science *374*, abg1727. 10.1126/science.abg1727.
3. Pasteels, J. (1937). Etudes sur la gastrulation des Vertébrés méroblastiques. III. Oiseaux. IV. Conclusions générales. Arch.Biol. *48*, 381-488.
4. Gont, L.K., Steinbeisser, H., Blumberg, B., and de Robertis, E.M. (1993). Tail formation as a continuation of gastrulation: the multiple cell populations of the Xenopus tailbud derive from the late blastopore lip. Development *119*, 991-1004.
5. Catala, M., Teillet, M.A., and Le Douarin, N.M. (1995). Organization and development of the tail bud analyzed with the quail- chick chimaera system. Mech.Dev *51*, 51-65.
6. Hatada, Y., and Stern, C.D. (1994). A fate map of the epiblast of the early chick embryo. Development. *120*, 2879-2889.
7. Psychoyos, D., and Stern, C.D. (1996). Fates and migratory routes of primitive streak cells in the chick embryo. Development. *122*, 1523-1534.
8. Tam, P.P., and Behringer, R.R. (1997). Mouse gastrulation: the formation of a mammalian body plan. Mech Dev *68*, 3-25.
9. Charrier, J.B., Teillet, M.A., Lapointe, F., and Le Douarin, N.M. (1999). Defining subregions of Hensen's node essential for caudalward movement, midline development and cell survival. Development *126*, 4771-4783.
10. Catala, M., Teillet, M.A., De Robertis, E.M., and Le Douarin, M.L. (1996). A spinal cord fate map in the avian embryo: while regressing, Hensen's node lays down the notochord and floor plate thus joining the spinal cord lateral walls. Development. *122*, 2599-2610.
11. Rosenquist, G.C. (1966). A radioautographic study of labeled grafts in the chick blastoderm. Development from primitive-streak stages to stage 12. Contr. Embryol. Carnegie Inst. Wash. *38*, 71-110.
12. Nicolet, G. (1970). Analyse autoradiographique de la localisation des differentes ebauches presomptives dans la ligne primitive de l'embryon de poulet. J. Embryol. Exp. Morph. *23*, 79-108.
13. Nicolet, G. (1971). Avian gastrulation. Adv Morphog *9*, 231-262.
14. Iimura, T., Yang, X., Weijer, C.J., and Pourquie, O. (2007). Dual mode of paraxial mesoderm formation during chick gastrulation. Proc Natl Acad Sci USA *104*, 2744-2749.
15. Wymeersch, F.J., Huang, Y., Blin, G., Cambray, N., Wilkie, R., Wong, F.C., and Wilson, V. (2016). Position-dependent plasticity of distinct progenitor types in the primitive streak. eLife *5*. 10.7554/eLife.10042.
16. Cambray, N., and Wilson, V. (2002). Axial progenitors with extensive potency are localised to the mouse chordoneural hinge. Development *129*, 4855-4866.
17. Cambray, N., and Wilson, V. (2007). Two distinct sources for a population of maturing axial progenitors. Development *134*, 2829-2840.

18. Garcia-Martinez, V., Alvarez, I.S., and Schoenwolf, G.C. (1993). Locations of the ectodermal and nonectodermal subdivisions of the epiblast at stages 3 and 4 of avian gastrulation and neurulation. J Exp Zool *267*, 431-446.
19. Brown, J.M., and Storey, K.G. (2000). A region of the vertebrate neural plate in which neighbouring cells can adopt neural or epidermal fates. Curr Biol *10*, 869-872.
20. Selleck, M.A., and Stern, C.D. (1991). Fate mapping and cell lineage analysis of Hensen's node in the chick embryo. Development. *112*, 615-626.
21. Spratt Jr., N.T. (1955). Analysis of the organizer center in the early chick embryo. I. Localisation of prospective notochord and somite cells. J.Exp.Zool. *128*, 121-162.
22. Guillot, C., Djeffal, Y., Michaut, A., Rabe, B., and Pourquie, O. (2021). Dynamics of primitive streak regression controls the fate of neuromesodermal progenitors in the chicken embryo. eLife *10*. 10.7554/eLife.64819.
23. Tzouanacou, E., Wegener, A., Wymeersch, F.J., Wilson, V., and Nicolas, J.F. (2009). Redefining the progression of lineage segregations during mammalian embryogenesis by clonal analysis. Dev Cell *17*, 365-376. 10.1016/j.devcel.2009.08.002.
24. Tam, P.P., and Beddington, R.S. (1987). The formation of mesodermal tissues in the mouse embryo during gastrulation and early organogenesis. Development *99*, 109-126.
25. Spratt Jr., N.T. (1947). Regression and shortening of the primitive streak in the explanted chick blastoderm. J Exp Zool *104*, 69-100.
26. Schoenwolf, G.C., Garcia-Martinez, V., and Dias, M.S. (1992). Mesoderm movement and fate during avian gastrulation and neurulation. Dev Dyn. *193*, 235-248.
27. Selleck, M.A., and Stern, C.D. (1992). Commitment of mesoderm cells in Hensen's node of the chick embryo to notocord and somite. Development *114*, 403-415.
28. Tonegawa, A., and Takahashi, Y. (1998). Somitogenesis controlled by Noggin. Dev Biol. *202*, 172-182.
29. Streit, A., and Stern, C.D. (1999). Mesoderm patterning and somite formation during node regression: differential effects of chordin and noggin. Mech Dev *85*, 85-96.
30. Hamburger, V., and Hamilton, H.L. (1992). A series of normal stages in the development of the chick embryo (1951). Dev.Dyn. *195*, 231-272.
31. Henrique, D., Abranches, E., Verrier, L., and Storey, K.G. (2015). Neuromesodermal progenitors and the making of the spinal cord. Development *142*, 2864-2875. 10.1242/dev.119768.
32. Furtado, M.B., Solloway, M.J., Jones, V.J., Costa, M.W., Biben, C., Wolstein, O., Preis, J.I., Sparrow, D.B., Saga, Y., Dunwoodie, S.L., et al. (2008). BMP/SMAD1 signaling sets a threshold for the left/right pathway in lateral plate mesoderm and limits availability of SMAD4. Genes Dev *22*, 3037-3049. 10.1101/gad.1682108.
33. Klein, A.M., Mazutis, L., Akartuna, I., Tallapragada, N., Veres, A., Li, V., Peshkin, L., Weitz, D.A., and Kirschner, M.W. (2015). Droplet barcoding for single-cell transcriptomics applied to embryonic stem cells. Cell *161*, 1187-1201. 10.1016/j.cell.2015.04.044.
34. Onichtchouk, D. (2016). Evolution and functions of Oct4 homologs in non-mammalian vertebrates. Biochim Biophys Acta *1859*, 770-779. 10.1016/j.bbagrm.2016.03.013.
35. Tyser, R.C.V., Mahammadov, E., Nakanoh, S., Vallier, L., Scialdone, A., and Srinivas, S. (2021). Single-cell transcriptomic characterization of a gastrulating human embryo. Nature *600*, 285-289. 10.1038/s41586-021-04158-y.

36. Guibentif, C., Griffiths, J.A., Imaz-Rosshandler, I., Ghazanfar, S., Nichols, J., Wilson, V., Gottgens, B., and Marioni, J.C. (2021). Diverse Routes toward Early Somites in the Mouse Embryo. Dev Cell *56*, 141-153 e146. 10.1016/j.devcel.2020.11.013.
37. Vermillion, K.L., Bacher, R., Tannenbaum, A.P., Swanson, S., Jiang, P., Chu, L.F., Stewart, R., Thomson, J.A., and Vereide, D.T. (2018). Spatial patterns of gene expression are unveiled in the chick primitive streak by ordering single-cell transcriptomes. Dev Biol *439*, 30-41. 10.1016/j.ydbio.2018.04.007.
38. Pijuan-Sala, B., Griffiths, J.A., Guibentif, C., Hiscock, T.W., Jawaid, W., Calero-Nieto, F.J., Mulas, C., Ibarra-Soria, X., Tyser, R.C.V., Ho, D.L.L., et al. (2019). A single-cell molecular map of mouse gastrulation and early organogenesis. Nature *566*, 490-495. 10.1038/s41586-019-0933-9.
39. Schiebinger, G., Shu, J., Tabaka, M., Cleary, B., Subramanian, V., Solomon, A., Gould, J., Liu, S., Lin, S., Berube, P., et al. (2019). Optimal-Transport Analysis of Single-Cell Gene Expression Identifies Developmental Trajectories in Reprogramming. Cell *176*, 928-943 e922. 10.1016/j.cell.2019.01.006.
40. Loulier, K., Barry, R., Mahou, P., Le Franc, Y., Supatto, W., Matho, K.S., Ieng, S., Fouquet, S., Dupin, E., Benosman, R., et al. (2014). Multiplex cell and lineage tracking with combinatorial labels. Neuron *81*, 505-520. 10.1016/j.neuron.2013.12.016.
41. Serra, M., Streichan, S., Chuai, M., Weijer, C.J., and Mahadevan, L. (2020). Dynamic morphoskeletons in development. Proc Natl Acad Sci U S A *117*, 11444-11449. 10.1073/pnas.1908803117.
42. Benazeraf, B., Beaupeux, M., Tchernookov, M., Wallingford, A., Salisbury, T., Shirtz, A., Shirtz, A., Huss, D., Pourquie, O., Francois, P., and Lansford, R. (2017). Multi-scale quantification of tissue behavior during amniote embryo axis elongation. Development. 10.1242/dev.150557.
43. Lange, M., Bergen, V., Klein, M., Setty, M., Reuter, B., Bakhti, M., Lickert, H., Ansari, M., Schniering, J., Schiller, H.B., et al. (2022). CellRank for directed single-cell fate mapping. Nature methods *19*, 159-170. 10.1038/s41592-021-01346-6.
44. Wagner, D.E., and Klein, A.M. (2020). Lineage tracing meets single-cell omics: opportunities and challenges. Nat Rev Genet *21*, 410-427. 10.1038/s41576-020-0223-2.
45. VanHorn, S., and Morris, S.A. (2021). Next-Generation Lineage Tracing and Fate Mapping to Interrogate Development. Dev Cell *56*, 7-21. 10.1016/j.devcel.2020.10.021.
46. Fulton, T., Verd, B., and Steventon, B. (2022). The unappreciated generative role of cell movements in pattern formation. R Soc Open Sci *9*, 211293. 10.1098/rsos.211293.
47. Hayward, M.K., Muncie, J.M., and Weaver, V.M. (2021). Tissue mechanics in stem cell fate, development, and cancer. Dev Cell *56*, 1833-1847. 10.1016/j.devcel.2021.05.011.